Article type : Original Manuscript

Corresponding author email id : kenya.ono@inpex.co.jp

Froude supercritical flow processes and sedimentary structures: New insights from experiments with a wide range of grain sizes

Kenya Ono[1,2], Piret Plink-Björklund[1], Joris T. Eggenhuisen[3] and Matthieu J.B. Cartigny[4]

[1]Geology and Geological Engineering, Colorado School of Mines, Golden, CO, United States. [2]INPEX Corporation, Tokyo, Japan. [3]Utrecht University, Utrecht, Netherlands. [4]Department of Geography, Durham University, Durham, United Kingdom.

Associate Editor – Alexandre Normandeau

Short Title – Supercritical flow sedimentary structures

ABSTRACT

Recognition of Froude supercritical flow deposits in environments that range from rivers to the ocean floor has triggered a surge of interest in their flow processes, bedforms and sedimentary structures. Interpreting these supercritical flow deposits is especially important because they often represent the

most powerful flows in the geological record. Insights from experiments are key to reconstruct palaeo-flow processes from the sedimentary record. So far, all experimentally produced supercritical flow deposits are of a narrow grain-size range (fine to medium sand), while deposits in the rock record often consist of a much wider grain-size distribution. This paper presents results of supercritical-flow experiments with a grain-size distribution from clay to gravel. These experiments show that cyclic step instabilities can produce more complex and a larger variety of sedimentary structures than the previously suggested backsets and 'scour and fill' structures. The sedimentary structures are composed of irregular lenses, mounds and wedges with backsets and foresets, as well as undulating planar to low-angle upstream and downstream dipping laminae. The experiments also demonstrate that the Froude number is not the only control on the sedimentary structures formed by supercritical-flow processes. Additional controls include the size and migration rate of the hydraulic jump and the substrate cohesion. This study further demonstrates that Froude supercritical flow promotes suspension transport of all grain sizes, including gravels. Surprisingly, it was observed that all grain sizes were rapidly deposited just downstream of hydraulic jumps, including silt and clay. These results expand the range of dynamic mud deposition into supercritical-flow conditions, where local transient shear stress reduction rather than overall flow waning conditions allow for deposition of fines. Comparison of the experimental deposits with outcrop datasets composed of conglomerates to mudstones, shows significant similarities and highlights the role of hydraulic jumps, rather than overall flow condition changes, in producing lithologically and geometrically complex stratigraphy.

Key words: Cyclic steps, Froude supercritical flow deposits, foreset and backset, gravel lenses, scour and fill, sedimentary structure hierarchy, upward fining stratigraphy.

INTRODUCTION

The recognition that Froude supercritical flows are more common and occur in a wider variety of environments than previously realized has recently increased interest in Froude supercritical flow processes, bedforms and sedimentary structures. Froude supercritical flow deposits are suggested to be common on modern and ancient active margin slopes (e.g. Walker, 1967; Komar, 1971; Hand, 1974; Migeon et al., 2000; Fildani et al., 2006; Postma et al., 2009, 2014, 2016; Paull et al., 2010;

Covault et al., 2014, 2017; Ito et al., 2014; Normandeau et al., 2014; Postma & Cartigny, 2014; Symons et al., 2016; Lang et al., 2017; Ono & Plink-Björklund, 2018;) and some basin floor fans (e.g. Walker, 1967; Migeon et al., 2000; Nakajima & Satoh, 2001; Normark et al., 2002; Postma et al., 2014; Postma & Kleverlaan, 2018). Supercritical flow is further considered to be the geomorphologically formative flow in flood-prone variable discharge rivers (e.g. McKee et al., 1967; Williams, 1971; Frostick & Reid, 1977; Foley, 1978; Tunbridge, 1981; Stear, 1985; Abdullatif, 1989; Bromley, 1991; North & Taylor, 1996; Alexander et al., 2001; Fielding, 2006; Billi, 2007; Fielding et al., 2009; 2018; Plink-Björklund, 2015; 2018). Supercritical flow deposits have also been described from a variety of other depositional environments, such as deltas (Massari, 1996; Ventra et al., 2015; Dietrich et al., 2016; Hughes Clarke, 2016), carbonate ramps (Massari & Chiocci, 2006; Lüdman et al., 2018; Slootman et al., 2019), glacial settings (e.g. Russell & Arnott, 2003; Duller et al., 2008; Lang & Winsemann, 2013; Lang et al., 2017) and volcanic settings (Schminke et al., 1973; Casalbore et al., 2014; Pope et al., 2018; Clare et al., 2018). Despite this recent surge of interest in Froude supercritical flow deposits and processes, sedimentologists struggle with interpreting the sedimentary structures within such deposits. The common long wavelength and low amplitude (e.g. Alexander et al., 2001; Cartigny et al., 2014) of supercritical-flow sedimentary structures make their recognition difficult, especially in outcrops of limited size. Furthermore, sedimentary structures associated with supercritical flows commonly display a wider range of structures compared to the subcritical-flow structures such as lower flow regime planar laminations, and primarily cross-lamina and cross-strata formed by migration of ripples and dunes (e.g. Allen, 1982; Baas, 2003).

Direct field observations (e.g. Normandeau et al., 2014; Fricke et al., 2015; Hughes Clarke, 2016; Hage et al., 2018; Normandeau et al., 2018), experimental studies (e.g. Simons & Richardson, 1961; Alexander et al., 2001; Spinewine et al., 2009; Yokokawa et al., 2010; Balmforth & Vakil, 2012; Cartigny et al., 2014; Fedele et al., 2016) and numerical models (e.g. Kubo & Nakajima, 2002; Fagherazzi and Sun, 2003; Kostic & Parker, 2006; Fildani et al., 2006; Vellinga et al., 2017), supply valuable tools for interpreting the sedimentary record, but are still relatively sparse. Furthermore, all experimental supercritical flow deposits have been produced in a narrow range of grain sizes, where median grain size is fine to coarse sand (0.12 to 0.60 mm) (Gilbert 1914; Guy et al., 1966; Kennedy 1961; Guy et al., 1966; Mastbergen & Winterwerp, 1987; Alexander et al., 2001; Spinewine et al.,

2009; Yokokawa et al., 2010; Cartigny et al., 2014; Fedele et al, 2016). In some cases (Cartigny et al., 2014), the grain size was so homogenous that it prevented the formation of visible stratifications and laminations that are encountered in natural deposits. While such studies have been instrumental in establishing the flow processes and bedform dynamics of supercritical flow regimes, they are of limited use to a sedimentologist in the field who aims to interpret sedimentary structures.

This study shows the results of flume experiments with sediment grain sizes from clay to gravels. These experiments demonstrate that a variety of sedimentary structures can be formed by cyclic step instabilities, rather than just backsets or 'scour and fill' structures. It is further shown here that the size and the migration rate of hydraulic jumps are significant controls on the sedimentary structures together with the available grain-size distribution. The experiments reveal that all grain sizes (including gravel) are transported in suspension and a subject to rapid local deposition at hydraulic jumps (including clay and silt). The similarity of these experimental deposits with outcrop datasets that have a grain-size range from conglomerates to mudstones and display significant stratigraphic and lithological complexity are discussed.

EXPERIMENTAL SETUP

Experiments were carried out at the Eurotank Flume Laboratory of the Utrecht University, mostly following the methodology of Cartigny et al. (2014) (Fig. 1). The experimental flume was 12.0 m long, 0.48 m wide and 0.6 m deep. It was filled with water and *ca* 1.5 m^3 of sediment, resulting in *ca* 0.2 m thick deposit on the flume floor with a water column of *ca* 3 to 10 cm on the sediment surface. Both sediment and water were recirculated by a pump. The flume was initially filled with only fine-grained sands (D_{50} = 146μm; Fig. 2). An electromagnetic discharge meter in the recirculation pipe measured the discharge. The discharge was set at one of two different values; high discharge (54 ± 2 m^3/h) and low discharge (49 ± 2 m^3/h) ranges. Eleven runs were conducted with variable discharge, sediment amount and grain size. Kaolin (D_{50} = 3.3 μm) was used for clay fraction, crushed glass (D_{50} = 31μm) for silt, poorly sorted medium to coarse-grained sands (D_{50} = 428 μm) and granules (2 to 3 mm) (Fig. 2 and Table 1). The materials of these grain-size classes were chosen to be visually distinct from the original fine-grained sands (Fig. 3) to ensure that sedimentary structures would be visible. These original fine-grained sands are yellowish-white, whereas the medium to coarse-grained sands

and the gravels are black to brown in colour. The whitish kaolin and silt provide an off-white hue when mixed with fine-grained sands.

In the experimental runs sediments were fed from the sediment feeder at a certain rate for 10 to 40 min, and individual runs lasted for 0.5 to 4.0 hours. The amount of sediment corresponding to what was added during the previous run was removed to keep the sediment budget constant in the flume (Table 1). Thus, the composition of the sediment in the flume became increasingly broader in grain-size range over the duration of the experiment (Fig. 3). A digital camera (Canon EOS 1100D; Canon, Tokyo, Japan) was placed at the side of the flume *ca* 6 m downstream of the inlet and 4 m downstream of the sediment feeding point, where it captured the flow dynamics and depositional processes through the glass wall of panel 6 (Fig. 1) every 2 seconds. The upstream panels 3, 4 and 5 were used to observe large-scale flow structures and the evolution of migrating bedforms. Therefore, the bedforms were observed on the two-dimensional flow parallel section only.

EXPERIMENTAL RUNS

All runs were dominated by the long wavelength instabilities associated with cyclic steps, as indicated by the distribution of the Froude numbers (Fr_{90} =1.59 to 2.34 and Fr_{50} = 0.66 to 0.99 in Fig. 4) (see also Cartigny et al., 2014). Although some additional short wavelength antidune instabilities were observed (see panel 3 in Fig 5.) between the hydraulic jumps. These antidunes did not impact the sedimentary structures presented here because the following hydraulic jump always reworked those structures that only occur at the very top of the cyclic step sequences. The first two runs, 1 and 2, were conducted for the reference of low and high discharge conditions, respectively. These conditions were used to decide discharge rates for relatively stable occurrence of hydraulic jumps (Figs 4 to 6). In this paper, only runs with the high discharge rate (52 to 56 m^3/h) are documented, as these runs formed larger structures which were easy to observe. Hydraulic jumps of the control run 2 occurred every 120 to 230 seconds in panel 6, and the peaks of Froude number frequently exceeded 2 (Fig. 4).

Medium to coarse-grained sands and gravels were added during runs 4 and 5 (Fig. 3). In both of these runs, coarser grained laminations formed in the fine-grained sand deposits within panel 6. In run 4, the coarser sands started to show up in panel 6 as brownish laminations 24 min after the start of

adding the coarser grains; and in run 5 they arrived 30 min after the start of feeding. Especially, in run 5, the coarse grains formed clear laminations (Figs 3 and 5).

In runs 6 to 9 silt was added. Some of the silt mixed into the sand and formed whitish laminae along scour surfaces (Figs 3 and 7A). The silt fraction component in sediment is significant as seen by grain-size distribution, as compared to run 4 (Fig. 7B). In run 6, visually diffuse whitish laminae formed, and the laminae were more distinct in runs 7 and 9 (Figs 3 and 7A). A few millimetre thick silty laminae were especially visible on erosion surfaces along the basal scours. Silt had a limited impact on the visible bedform architecture, or on the occurrence of hydraulic jumps that look very similar to those of run 2 (Fig. 4C).

Kaolin clay was added in runs 10 and 11 (Fig. 3). Hydraulic jumps of run 11 occurred every 160 to 370 seconds. This is a longer recurrence interval compared to the control run 2 (Fig. 4D) and suggests that clay content influences the length or the migration velocity of the bedforms. Kaolin also provided more cohesion, and transient steeper irregular slopes caused local slumping (Fig. 7C).

GENERAL MORPHODYNAMICS

Basic morphodynamics of the dominant cyclic step instabilities are well-illustrated by the continuous panel views of runs 5 and 9 (Figs 5 and 6). Bedform surfaces have a characteristic undulating geometry (see also Spinewine et al., 2009; Yokokawa et al., 2009; Cartigny et al., 2011). Hydraulic jumps occur in the troughs between the crests, where supercritical flow transforms into subcritical flow. Upstream of the hydraulic jump the surface dips downstream on the lee side of the bedform. This surface is formed by erosion due to the acceleration of the flow toward the hydraulic jump. At the hydraulic jump, the flow velocity drops drastically and the flow thickness increases. The underflow (lower jet flow of Fedele et al., 2016) maintains high velocity and erodes the substrate, followed by quick deceleration downstream, where deposition becomes dominant (see panel 4 in Fig. 5). Due to the rapid deposition, the underflow erosion surface at the hydraulic jump is instantaneously preserved. This surface exhibits flat to concave-up scour geometry. Downstream of the hydraulic jump, flow accelerates towards the top of the bedform crest, where the flow gradually transforms into supercritical flow through transcritical flow conditions. At this transition point from subcritical to supercritical flow, erosion becomes dominant and most of the sediment becomes suspended, including

the gravels. Directly downstream of the hydraulic jump and within the subcritical zones, some bedload transportation occurs together with rapid deposition. Deposition downstream of the hydraulic jump, and erosion upstream of the hydraulic jump are coeval (Figs 5 and 6). As the hydraulic jump migrates upstream, the location of deposition and erosion shifts, and the high deposition rate facies (structureless or normally graded deposits) and the coarsest grain sizes are spatially closely associated with the basal erosion surfaces in both vertical and lateral directions.

The size of the hydraulic jumps varied spatially and temporally (Fig. 4), even though the flow discharge rate was not varied during the experiments. Hydraulic jump sizes have been described as the ratio of Froude numbers before and after the hydraulic jump (e.g. Chow, 1959; Cartigny et al., 2014) (Fig. 4). Visual observations in this experiment show that the water surface difference upstream and downstream of the hydraulic jump and the scour depth are also related to the Froude number ratio (Fig. 8). Large hydraulic jumps have a Froude number range and ratio of *ca* 2 to 5 ($Fr_{\text{before hydraulic jump}} - Fr_{\text{after hydraulic jump}}$) and *ca* 5 to 20 ($Fr_{\text{before hydraulic jump}} / Fr_{\text{after hydraulic jump}}$) and small hydraulic jumps *ca* 1 to 2 and up to 5 (Fig. 4). Large hydraulic jumps have a water surface difference of 5 to 20 cm and scour depth of 4 to 15 cm, and small jumps 2.5 to 5.0 cm and a few centimetres respectively (Figs 5, 6 and 8). Although the long-term aggradation condition was not reproduced, the short-term aggradation repetitively occurred in this experiment. The large hydraulic jumps occasionally eroded down to the bottom of the flume, and were followed by rapid sediment aggradation. The small hydraulic jumps reworked only shallow horizons. Over the three panels (Figs 5 and 6), across 3 m, this lateral variability of supercritical flow and its interaction with sediment is clearly visible.

MORPHODYNAMICS OF SPECIFIC BEDFORMS AND THEIR SEDIMENTARY STRUCTURES

Flow interaction with gravels

The gravelly sedimentary structures display a larger degree of complexity as compared with sedimentary structures formed in fine-grained sands (Figs 3 and 5B). The structures exhibit not only the previously described upstream (backset) and downstream dipping (foreset) laminae with erosionally truncated surfaces, and also form mound and wedge shapes, consistent backset trains and amalgamated lenses (Figs 5B, 6C, 9C, 9D and 10C).

Mound and wedge-shaped structures

Mound-shaped gravelly stuctures form through rapid deposion of gravels provided by repetitive surges from transiently stationary hydraulic jumps (Fig. 9). The basal undulating erosion surface forms as an unsteady hydraulic jump migrates by with an irregular migration velocity (t_1 = 0 s in Fig. 9A). Erosion occurs where the hydraulic jump becomes temporarily stationary or during periods when the hydraulic jump becomes larger. The passage of the hydraulic jump is followed by deposition of sands and gravels on the upstream dipping side of the hydraulic jump scour (t_2 = 6 s in Fig. 9A). Gravels fall out closer to the hydraulic jump, as compared to sands, due to their higher settling velocity, and form an initial triangular mound. A deep scour forms at the right edge of panel 6 (t_3 = 24 s in Fig. 9A), as the hydraulic jump becomes stationary. The newly arriving gravels fall out from hydraulic jump and accrete onto the initial mound, forming backsets as well as foresets. The foresets grade downstream from gravel to sand, as the sands are deposited further downstream. As the hydraulic jump migrates further upstream, the mound-shaped gravel bedform is rapidly overlain by fine-grained sands and preserved (t_4 = 120 s in Fig. 9A). The foresets and backsets have a dip angle up to 20° and flank the initial triangular shaped mound. The foresets show a fining (sandying) upward trend. The backsets show a sigmoidal accretion pattern and do not have grain-size trends (Fig. 9B and C). Between t_4 and t_5, a small hydraulic jump migrates upstream (Fig. 9A), but does not erode down into the gravel bedforms.

The partial erosion of mound-shaped structure leads to wedge-shaped structures (Fig. 9). The upstream migrating hydraulic jump that caused deposition of the consistent backsets continuously erodes the top of the previously deposited gravel mound in the right corner of panel 6 (t_5 = 378 s in Fig. 9A). The upstream dipping strata of the mound located in a deeper part of the hydraulic jump scour are preserved. They form a wedge-shaped stucture that is bound by a sharp downstream dipping erosion surface and contains upstream dipping sigmoidal laminae (Fig. 9D).

Consistent backsets

Consistent backset structures exhibit regular upstream inclined strata and form during stable upstream migration of hydraulic jumps. Following the above described sequencial process in run 5 (Fig. 9), a

third hydraulic jump migrates upstream at a stable rate and forms a relatively flat erosion surface (t_5 = 378 s in Fig. 9A). This hydraulic jump erodes the gravel mound and redeposits some of the gravel on the flat surface. This pulsed redeposition of gravels is followed by continuous accumulation of fine-grained sands with a relatively sharp grain-size decrease on the top of the gravel bedform. The fine sands form low-angle undulating laminae. Continued stable upstream migration of the hydraulic jump causes gradual deposition of regular gravel backsets as their depositional zone also migrates upstream (t_6 = 416 s in Fig. 9A). This gravel bedform is preserved as a flat based set of gently dipping (up to 10°) backsets, abruptly overlain by fine-grained laminated sands (Fig. 9D).

Amalgamated lens-shaped structures

Amalgamated lens-shaped structures are compound gravel lenses formed by repeated formation of gravel mounds and their gravitational reworking during surges from the underflow of transiently growing hydraulic jumps in steep scours. The amalgamated mounds (Fig. 10) form 83 min (5000 sec) later in run 5 as shown by time steps in Fig. 10A. An upstream migrating hydraulic jump erodes the above described bedfroms ($t_{1–2}$ = 0 to 8 s in Fig. 10A). When the hydraulic jump becomes stationary ($t_{2–4}$ = 8 to 14 s in Fig. 10A) a deep scour forms, its surge provides gravels that are deposited on the upstream facing side of the hydraulic jump scour and form an elongate mound. This mound deposition is followed by gravitational emplacement of some of the gravels down the steep scour slope towards the base of the scour ($t_{4–5}$ = 14 to 16 s in Fig. 10A). The next surge of gravels forms a new mound that consists of backsets and foresets ($t_{6–8}$ = 18 to 24 s in Fig. 10A) higher on the upstream facing scour of the hydraulic jump, as the hydraulic jump gradually becomes larger and more stationary. This mound also becomes unstable due to rapid accumulation, and some of the gravels slide down to the base of the scour (t_9 = 28 s in Fig. 10A). Upstream migration of the hydraulic jump provides a new surge of gravels ($t_{10–11}$ = 32 to 34 s in Fig. 10A) that form a third lens, followed by rapid sand deposition. The preserved bedform consists of three stacked gravel lenses bounded by upstream facing steep erosion surfaces (up to 20°) (Fig. 10C). Individual lenses contain backsets or foresets or both, where the gravitationally redeposited gravels are internally structureless. The foresets are more gently dipping (from a few to 10°) and have concave shapes (Fig. 10C). The

initial hydraulic jump scour surface forms a compound basal erosion surface for the three lenses (Fig. 10C).

Summary

In summary, the gravelly sedimentary structures are a function of gravel availability, gravel settling velocities, and the size and migration rate of the hydraulic jumps. Gravel availability is quickly transformed from a stable feeder supply upstream to a stepwise supply, because all gravel is temporarily deposited downstream of the first hydraulic jump. A passage of a subsequent hydraulic jump erodes gravels and suspends them, and they are deposited successively just downstream of the hydraulic jump, at the upstream facing side of the hydraulic jump scour due to their high settling velocities. Thus, although the gravels are suspended while transported, their downstream movement is episodic and depends on the passage of hydraulic jumps. The lateral relationship of the gravelly structures with sands, and the resultant complexity of the gravel–sand sedimentary structures are determined by the gravel settling velocity, hydraulic jump size and the hydraulic jump migration rate. The hydraulic jump migration rate also determines the shape of the sedimentary structures as steady hydraulic jump migration produces flat erosion surfaces and consistent backsets, whereas unsteady hydraulic jumps' migration and stationarity form concave-up scours, mound, wedge-shaped structures and amalgamated scour-bound lenses. Backsets also form on the upstream-facing side of the mounds, whereas foresets form where gravels are transported just beyond the mound. These gravelly foresets then fine into sands. The complexity of the sedimentary structures is further increased by partial erosion (wedge-shaped gravelly structures) and gravitational redeposition (amalgamated lenses). All gravelly structures were rapidly covered by sands when the hydraulic jumps migrated further upstream, and would thus have been preserved during shorter events or under more aggradational conditions.

Flow interaction with silt

Silt alone had a limited impact on the bedform architecture or on the occurrence of hydraulic jumps, because they look very similar to those of the control run 2 (Figs 3 and 4). The experiments demonstrate that silt can be deposited from supercritical flow instabilities, due to the rapidly

decreasing bed shear stress downstream of a hydraulic jump, rather than from waning-stage flow only, as commonly considered (e.g. Bouma, 1962; Lowe, 1982; Sumner et al., 2012). Some of the silts are deposited together with fine sand and thus contained as the matrix in the fine-grained sand (Fig. 7B). Some silt can also be observed in deeper parts of scours as thin, a few millimetre-thick laminations (Fig. 11), and in upper parts as a cm-thick diffuse low-angle lamination (Fig. 7A). The small proportion of distinct silt laminae in deeper parts may further be a result of rapid post-depositional water escape. The diffuse lamination in upper parts are deposited under the subcritical to transcritical flow phase in the stoss side of hydraulic jump (Fig. 6A and B).

Flow interaction with clay

Adding kaolin clay (Fig. 2) to the experiment in run 11 affected the flow morphodynamics by producing initially steeper but successively longer and shallower hydraulic jump scours associated with longer migration periods. The resultant sedimentary structures were characterized by normal grading of gravels, loading structures and lower-angle laminae and lenses (Fig. 12). These heterolithic bedforms were observed to form during the passage of two cyclic step instabilities (Fig. 12A), as seen in a time series (Fig. 12A). Kaolin is deposited together with sands and produces cohesive and less permeable and water-rich deposits. These bed properties seem to initially promote locally steeper scour surfaces at the hydraulic jump (t_1 = 0 s in Fig. 12A; see also Fig. 7C). Due to cohesive gravitational deformation and the continued erosion of the upstream side of the hydraulic jump, these steep surfaces are not preserved and the erosion surface formed by the migrating hydraulic jump becomes relatively shallow and long. As gravel-rich coarser sands arrive, they are deposited and loaded into the clay-rich substrate (t_2 = 12 s in Fig. 12A). Due to loading, gravels form concave lenses rather than mounds. As the relatively initially stationary hydraulic jump starts quickly migrating upstream (t_3 = 22 s in Fig. 12A), a step-like irregular scour surface forms. During the upstream migration of the hydraulic jump, successively finer grain sizes are deposited and form normally graded gravels (t_4 = 48 s in Fig. 12A). Rapid sand deposition over the gravelly lenses produces a fining upward trend of the whole scour fill, where gravels are clearly normally graded, but fine-grained sands overlay the gravels with a sharp grain-size shift and display only weak grading (t_5 = 102 s in Fig. 12A). The next migrating hydraulic jump erodes into the gravel layer at the centre of the

panel and forms isolated lenses (t_6 = 384 s in Fig. 12A). The eroded gravels are transported onto the downstream edge of the scour. The surge of the migrating hydraulic jump provides a new population of coarse grains that form 2 to 3 cm deep loading structures with irregular basal surfaces (t_7 = 400 s in Fig. 12A). During further hydraulic jump migration fine sands quickly cover the coarse lenses (t_8 = 502 s in Fig. 12A).

Unique to this run are the normally graded gravels and isolated normally-graded gravel lenses loaded into the substrate. The loading structures are 2 to 3 cm deep and form a highly irregular basal surface (Fig. 12B and C). Gravel lenses are a few centimetres thick, and overlain by fine-grained sand with a sharp grain-size shift (Fig. 12D). It is also characteristic that the hydraulic jump scours were more elongated and shallower, and that the migration period of hydraulic jumps was longer (Fig. 4D). A key outcome of this portion of the experiment (runs 10 and 11) is that clay and silt can be deposited in hydraulic jumps and interbedded with sands and gravels. These results expand the range of dynamic mud deposition into the supercritical flow.

KEY CONTROLS ON SEDIMENTARY STRUCTURES

The general nature of the sedimentary structures of these experiments is in good agreement with previous experiments (Alexander et al., 2001; Cartigny et al., 2014) and confirms again the abundance of concave-up laminae dipping upstream and downstream, and convex-up laminae filling troughs (Fig. 13). However, the wider grain-size distribution enables some aspects of flow and sediment interaction to be observed in greater detail. Based on these observations it is suggested that the resultant sedimentary structures are strongly controlled by variations in the strength, stability and migration rate of the hydraulic jumps (Table 2). This result is an experimental confirmation of the prediction of the importance of hydraulic jump variability based on numerical modelling by Vellinga et al. (2017). The observations herein also highlight the suspension transport of all grain sizes and the differences in flow interaction with different grain-size classes. This study also shows that cyclic step instabilities can produce more complex and a larger variety of laminations than previously suggested (e.g. Cartigny et al., 2014; Hage et al., 2018). The present experiments produced irregular lenses, mounds and wedges, as well as undulating planar to low-angle upstream and downstream dipping laminae (for example, Fig. 12), in addition to backsets and amalgamated scour and fill structures.

These experiments also show that grain sizes from gravel to clay fall out in close proximity in hydraulic jumps and have the potential to produce highly heterolithic and potentially cohesive deposits (see also Ono & Plink-Björklund, 2018).

Erosion–deposition dynamics

The experiments indicate that cyclic step instabilities enhance deposition and erosion to occur in bursts, where erosion on the supercritical lee side of the hydraulic jumps generates surges of sediment that are partially deposited in the vicinity of the hydraulic jump and partially transported further downstream. Erosion on the supercritical lee side and beneath the underflow within the hydraulic jump forms the composite erosion surface as previously described by Slootman et al., 2019 (Figs 5 and 6). Deposition starts in the vicinity of the hydraulic jump where supercritical flow transitions into subcritical flow (see also Winterwerp et al., 1992; Kostic & Parker, 2006; Cartigny et al., 2014; Vellinga et al., 2017). As a result, both maximum erosion rate and maximum deposition rate conditions are laterally closely associated as was also previously observed by Postma et al. (2009). This results in accumulation of deposits that indicate the highest deposition rates and have the coarsest grain sizes, such as coarse structureless or normally graded deposits, just above the basal erosional scour surfaces (Figs 6B and 12D). Infilling of this erosional scour results in upstream or downstream dipping, or upward flattening laminae with dip angles of up to 20° (Figs 5A, 6A, 9C, 9D and 12B).

Suspension transport and settling velocity

All grain sizes, including the gravels (2 to 3 mm) were transported in suspension (Figs 9A, 10A and 12A). The coarser material was systematically deposited closer to the hydraulic jump compared to fine sands. Thus, differences in settling velocities allow for grain-size segregation, as gravels and coarser sands settle first and form lenses above erosional scours. In contrast, fine-grained sand, silt and clay are deposited together, invoking that their settling velocities are not distinct enough at high sediment concentrations. Alternatively, initially deposition may be driven by competence (*sensu* Hiscott, 1994) because only the coarser clasts settle out, and this is followed downstream by capacity driven deposition where all grain sizes deposit into a structureless or weakly laminated facies. This is

consistent with the suspension capacity perspective proposed by Eggenhuisen et al. (2017), who predict that turbulent carrying capacity of suspended sediment is not determined by grain size for sediment smaller than 200 μm. This would explain why clay, silt and fine grained sand are deposited together, apparently without much grain-size segregation. Independent of the cause, the fine sands and silts form the structureless or weakly laminated facies that overlie normally graded gravel to coarse sand deposits with a sharp grain-size shift (Fig. 6B). It is also interesting that normal grading of gravels primarily occurs in the presence of clay, suggesting a significant effect of clay on flow rheology (Fig. 12D). Bedload transport only occurs locally and transiently as traction reworking of suspension fallout deposits.

Gravel transport

Gravels and coarse sands exhibit stepwise downstream movement, where their suspension transport is interrupted by fallout at hydraulic jumps. When added to the flume, the gravels and coarse sand were immediately deposited into a downstream trough, as their settling velocity is high. They were re-suspended by the scouring action of the underflow of a successive upstream migrating hydraulic jump, and re-deposited in the subcritical zone. Successive repetition of this process produces the stepwise downstream transport because, once deposited, gravels and coarse sands can be re-suspended only by increased shear stress caused by a successively migrating hydraulic jump. The gravel content becomes smaller downstream along the flume, as there is a 24 to 30 min gravel transit time to panel 6 due to the stepwise gravel movement that generates a time lag. Some gravel is trapped in the base of the deep scours. This stepwise movement and the trapping in deeper horizons produces lateral and vertical heterogeneity in sedimentary facies on relatively short spatial scales. Thus, gravel is likely to occur as lenses just above scour surfaces as controlled by gravel interaction with hydraulic jump migration.

Hydraulic jump size and migration rate

Observations across the three panels (Figs 5 and 6), also show that the size of the hydraulic jumps controls the shape and size of bedforms and their resultant deposits. Panel 5 in Fig. 5 and panel 3 in Fig. 6 show two relatively small hydraulic jumps (See Fig. 8 for definition) producing shallow scours

and low-angle undulating laminations. Similar low-angle laminations are also visible within the upper interval of deposits in Figs 5 and 6. Further upstream in panel 4 (Fig. 5) a large hydraulic jump forms a gravel mound and erodes deeply into precedent gravel deposits. Another example of a large hydraulic jump seen in panel 5 of Fig. 6 produces backsets that are steep and *ca* 10 cm in height. Examples of other large hydraulic jump deposits occur as scour-bound gravels with lenticular geometries which are erosionally or sharply bounded and enclosed in fine-grained sands (lower interval in Figs 5 and 6). These scours are 30 to 90 cm long and 10 to 15 cm deep, and display cross-cutting geometries. The well-preseved and extended scour length will be approximately 0.5 to 1.0 wavelength of the cyclic-step bedform (Fig. 6). Gravel lenses are not distributed homogeneously on the scour surfaces, but are rather deposited locally on the side of the scours with more steeply dipping surfaces (Figs 5B, 6B and 6C), and form upstream and downstream facing sigmoidal laminations. The scour fills show diffuse upward flattening laminations and look almost structureless in places (Fig. 6B).

Examination of the migration rate of the hydraulic jumps shows some variations between runs 2, 5, 9 and 11 as average migration rate varies 0.8 to 1.6 cm/s across panel 6 (Fig. 14). Most migration rates of individual hydraulic jumps show unsteady movement, seen as gradient changes in the plots in Fig. 14. This is consistent with observations of hydraulic jumps becoming temporarily stationary before accelerating again to higher migration rates (for example, Figs 9A, 10A and 12A). The migration rate of run 11 with clay displays higher irregularity and a wider range of migration rates compared to the other three runs (Fig. 14). It is concluded that migration rate irregularity is enhanced by the clay content (Fig. 14), because the clay significantly affects fluid properties (e.g. Baas et al., 2015) as well as forming a cohesive and deformable substrate (e.g. Baas et al., 2016). The hydraulic jump size variation does not have a clear relationship with migration rate.

This size and the migration rate variability is a key control on bedform morphodynamics and the resultant sedimentary structures. Large hydraulic jumps form deep scours with steep upstream and downstream faces because the migration rate of the hydraulic jumps is variable. The hydraulic jumps move upstream in a stepwise manner forming deeper scours where the migration rate is slow, and relatively shallow surfaces where the migration rate is high (Fig. 15). This results in irregular undulating erosion surfaces (t_1 in Fig. 9A and $t_{1–4}$ in Fig. 10A). When hydraulic jumps migrate at

stable rates, they form flat erosion surfaces (t_5 in Fig. 9A), and consistent upstream dipping laminae or mound-shaped bedforms dependent on the shape of the scour and the migration rate of the hydraulic jump (Figs 9 and 10). Moreover, larger hydraulic jumps erode deeper, and form erosionally-bound and wedged-shaped deposits (t_5 in Fig. 9A). Small hydraulic jumps tend to form shallow scours, which when covered with sediments result in planar to undulating laminations, independent of the stability of the hydraulic jump migration (see panel 5 in Fig. 5A, panel 3 in Fig. 6A, and Fig. 6B and C). Small hydraulic jumps can also form local gravel mounds where they rework the precedent gravel mound deposits (see panels 3 and 4 of Fig. 6).

Cohesive substrate

Rapid deposition at hydraulic jumps causes rapid sediment fallout and mixes some of the kaolin into the fine sand, promoting significant loading in the cohesive kaolin containing substrate as the less permeable substrate captures more water from rapid deposition. This soft and deformable substrate also promotes gravitational sliding and reworking of scour surfaces (e.g. Baas et al., 2016). Thus, the passage of hydraulic jumps forms relatively shallow scours (Fig. 3, t_2 and t_7 in Fig. 12A). This causes gentler and longer wavelength cyclic step bedforms, perhaps further enhanced by a longer period of the hydraulic jumps (Fig. 4D). If a hydraulic jump becomes stationary, it does form deeper and more elongated scours, because the slumping prevents from preserving steeper scour surfaces (Fig. 7C). The cohesive substrate also has a significant effect on coarse-grained sedimentary structures as they form lenses rather than mounds, because they load into the substrate, as the gravel lenses have higher density than the substrate (e.g. Allen, 1982; Owen, 2003).

IMPLICATIONS FOR OUTCROP INTERPRETATION

Sedimentary structures produced in these experiments bear close similarity with field datasets of upper to middle slope turbidite deposits from the Eocene Juncal Formation and the La Jolla Group. These deposits contain grain sizes from cobbles to clay (Ono & Plink-Björklund, 2018), similar to those described in other coarse-grained turbidite outcrop datasets that expose a large range of grain sizes (e.g. Lowe 1982; Massari 1984; Ito & Saito, 2006; Postma et al., 2009; Ito, 2010; Ito et al., 2014; Postma et al., 2014). Specific aspects of the experimentally produced sedimentary structures

and their potential implications for outcrop interpretations are discussed below. However, the long term aggradating environments commonly observed in the deltas (e.g. Lang & Winseman, 2013; Slootman et al., 2019) are not considered here. Synthetic aggradation (Cartginy et al., 2014) would be needed to reproduce systematically climbing bedforms.

Lateral sedimentary structure variability and bedform stability fields

Despite the constant discharge and the dominance of cyclic steps, the experiments produced a wide range of sedimentary structures that range from low-angle undulating laminations to systematic backsets to 'scour and fill' structures as well as to mounds and wedges. This is in contrast to some previous hypotheses that suggest a prevalence of systematic backsets with reworking into scour and fill structures (e.g. Hage et al., 2018), or that low-angle undulating bedforms specifically indicate antidune deposition (e.g. Fielding, 2006). The present results rather support that a large variety of sedimentary structures can be produced from upstream migration of cyclic steps (*see also* Ito & Saito, 2006; Ito, 2010; Ito et al., 2014; Postma et al., 2014; Lang et al., 2017; Ono & Plink-Björklund, 2018), as a function of hydraulic jump size, migration rate and sediment calibre. The experiments show that plane beds and low-angle undulating beds form lateral to hydraulic jumps, coeval with the accretion of backsets, sigmoidal mound strata or scour and fill laminae (Figs 5, 6, 9B and 10B), rather than due to changes in overall flow regime. At the limited outcrop, these experiments thus caution against attempting to link specific outcrop sedimentary structures to specific supercritical flow bedform stability conditions, and support the notion that antidunes, unstable antidunes, chutes and pools and cyclic steps are mutually transitional bedforms (see Cartigny et al., 2014 and Fedele et al., 2016). However, the proportional dominance of steep backsets and deep scour fills over extensive outcrops can be used for identification of sustained occurrence of hydraulic jump and thus cyclic step bedforms.

The lateral sedimentary structure variability in such as those transitional bedforms is also common in the Juncal Formation and the La Jolla Group (Fig. 16). The conglomeratic deposits display complex amalgamated erosionally bound lenses with foreset and backset bedding, mound shaped and wedged-shaped gravels (Fig. 16A to C), as well as systematic backsets (Fig. 16D). Normal grading from cobble or pebble conglomerate to sandstone also occurs on tens of centimetres to a metre scale above basal scour surfaces (Fig. 16E). In places even disorganized conglomerates are

observed encased in organized conglomerates in scour fills, (Fig. 16F) similar to the gravitationally emplaced gravels in the experiments (Fig. 9C). Loading structures are recognized as a few metres deep irregular-shaped concave-up surfaces (Figs 12 and 16A). These sedimentary structures are similar to a variety of deposits produced in these experiments (Figs 9, 10 and 12) and display the characteristic lenticular shapes with upstream and downstream inclined surfaces, bounded by the master erosion surface formed by the passage of hydraulic jumps (Fig. 5B). The experiments also explain the common occurrence of flat or step-wise erosion surfaces (Fig. 16G), as a function of hydraulic jump migration rate and size.

Froude supercritical flow structures are commonly referred to as low-angle cross-strata (e.g. Fielding, 2009), in order to contrast with high-angle (up to 30°) dip of cross-strata produced by dunes or ripples (see also Alexander et al., 2001). The experiments herein produced some cross-strata that are relatively steep and have dip angles of up to 20°, similar to the experiments of Alexander et al. (2001). It is thus important to consider other differences in supercritical and subcritical flow cross-strata, such as that the here experimentally produced steeper supercritical flow cross-strata occur as erosionally bound lenses or wedges, or mounds that display both foresets and backsets, or asymmetrical scour fills with upward flattening of strata (Figs 5 and 6). In contrast, subcritical flow cross-strata occur as consistent cross-sets, and are thus most similar to the here produced consistent backsets (Figs 9D and 13B).

These experiments further highlight the ambiguity of interpreting structureless strata (see also Postma et al., 2009, in case of uniform grain sizes). Run 2 with fine sand only produced seemingly structureless strata formed by layer by layer stratification (run 2 in Fig. 3) rather than by *en masse* or freezing deposition, such as from a laminar flow (Talling et al., 2012) or from traction carpets (Sohn 1997; Postma et al., 2014).

Sedimentary structure hierarchy

There is more than an order of magnitude variation in the size of the documented hydraulic jumps and their consequent erosion surfaces (for example, scour depth and width) (Figs 4 and 8, see also discussion in Lang et al, 2017), despite the constant discharge. The experimental scour size varies from a few centimetres to 15 cm deep (Figs 5, 6 and 8). Similar, order of magnitude variability in

scour size is observed in the Juncal Formation and the La Jolla Group, where scours range from a sub-metre scale to more than 20 m deep (Fig. 17). The larger scours could easily be interpreted as channels rather than mesoforms (bedforms), and interpreted to reflect boundary condition changes (for example, waning flow) rather than as a single scour and fill structure produced at a steady discharge. For comparison, the channel size in the Juncal Formation and the La Jolla Group ranges from 30 to 90 m deep and 300 to 800 m wide.

Another example of hierarchical scale relationships of sedimentary structures is, for example, on Figs 5A and 6A that show several 60 cm to a metre long scours, with a few to 10 centimetre long coarse sand to gravel lenses, all formed by the passage of a hydraulic jump (Figs 9A and 10A). It is interesting that similar scale differences with a few tens of centimetres thick undulating convex-up to hummock-like structures on a few hundred metre sediment waves, were instead interpreted as smaller subcritical flow sedimentary structures on the larger supercritical flow structures in outcrops of channel-lobe transition zone (Hofstra et al., 2018).

Lateral and vertical grain-size variability

The experiments produced a high degree of lateral and vertical grain-size variability, because the coarse sands and gravels occur as mounds, lenses and graded intervals above major scour surfaces. Such occurrence of conglomerates above erosion surfaces in overall upward fining units (Figs 5 and 6) can easily be interpreted as channels or channel stories when up-scaled to outcrop, and linked to processes like channel initiation and backfilling. The experiments show that conglomerates are likely to occur above major erosion surfaces because of their rapid fallout rates just downstream of the hydraulic jumps, when they are re-suspended by hydraulic jump erosion, whereas sands are transported further. It is the upstream hydraulic jump migration that produces upward fining trends. Normal grading from gravel to sand was produced in experiments with clay and thus suggest an additional control on graded beds other than the sediment fallout rates. The Juncal Formation and La Jolla Group outcrops commonly display numerous examples of conglomerates laterally and vertically interbedded with sandstones as well as with siltstones (Figs 16 and 18), as well as upward fining trends (Fig. 17). Stratigraphic complexity is further enhanced by the lateral and temporal variability in hydaulic jump size (Figs 5A and 6A).

The experimentally produced upward-fining patterns are notably similar to the classical coarse-grained turbidites interpreted as waning flow deposits (e.g. Lowe, 1982; Massari, 1984; Mutti, 1992; also Bouma Ta facies of Bouma, 1962). This similarity was previously discussed by Postma et al. (2009; 2014), where these upward fining patterns are also linked to cyclic step migration. The idealized vertical successions of the classical coarse-grained turbidity current deposits (e.g. Lowe, 1982; Massari, 1984, Mutti, 1992) is also similar to the internal facies transitions from gravelly structureless to scour-fill facies and to more laminated sandier facies. The experiments herein suggest that such transitions could be linked to the migration of various-sized hydraulic jumps (Figs 6A, 6B and 13A), in addition to the previously proposed mechanism of single hydraulic jump migration and traction carpet formation (Postma et al., 2009; 2014). The hydraulic jump instabilities together with the variability in upstream eroded sediment calibre then determine the specific types of facies, such as crudely stratified gravels or coarse-tail graded facies (Fig. 12D and outcrop example in Postma et al., 2009), or inversely graded facies (Fig. 6C and outcrop example in Sohn, 1997), as well as the bounding erosion surfaces and facies stacking pattens (Figs 3, 5A and 6A and outcrop example in Postma et al., 2014), and the sharp grain-size shifts (Fig. 12D and outcrop example in Massari, 1984). Furthermore, the common downstream fining trends described from outcrops (e.g. Massari, 1984; Mutti 1992), and interpreted as downstream waning flow condition (e.g. Mutti et al., 2003), can also be linked to stepwised downstream gravel transport, which forms heterolithic but overall downstream fining trends in the experimental deposits (Figs 5A and 6A).

This study also observed downstream fining on individual bedforms scale, such as in gravelly mounds and lenses (for example, Figs 9 and 10). This grain-size trend may prove a useful flow direction indicator, because palaeocurrent measurements from supercritical flow deposits are ambiguous due to the presence of both foresets and backsets, as well as due to scour and fill structures that may be confused with a flow-perpendicular view of trough cross-strata.

Froude supercritical flow cyclic-steps in turbidity currents versus open channel flow regarding their flow processes and experimental setups

Although the experimental deposits were produced under open channel flow conditions, their similarity to the outcrop turbidity current deposits, but also to river deposits (see e.g. Wang & Plink-

Björklund, 2019; Zellman, 2019), is striking. According to the numerical models, flume experiments and direct turbidity current observations, Froude supercritical turbidity currents and open channel flow demonstrate similar bedform migration when forming cyclic steps (e.g. Sequeiros et al., 2010; Fedele et al., 2016; Hughes Clarke, 2016; Vellinga et al., 2017).

Viewing the subcritical flow bedforms in fluvial environments (e.g. Allen, 1982), bedload transport takes a significant role in the morphodynamics of the bedforms. This aspect is quite different from turbidity currents that are considered to be dominated by suspension transport. However, the open channel supercritical-flow flume and numerical experiments (Cartigny et al., 2014; Vellinga et al., 2018; this study) (Fig. 3 runs 2, 4 and 5; Fig. 5) exhibit significant suspension transport with a substantial sediment-concentrated layer at the basal part of the flow, potentially affecting the formation mechanism of supercritical flow bedforms. Furthermore, recent studies (Hughes Clarke et al., 2016; Symons et al, 2017; Paull et al., 2018) demonstrate that the modern sandy turbidity currents produce a dense basal layer that could be formed by a mixture of bedload and suspended load. This leads the authors to assume that flow dynamics are similar in supercritical turbidity currents and open channel flow.

There is also a feasibility issue with the turbidity current experiments, because in order to suspend sands the flow needs an extensive setup. Only the experiment by Jorristma (1973) has managed to produce cyclic steps in sandy turbidity currents in a flume that was over 30 m long. It would be challenging and costly to operate such facilities, and the flow cannot be maintained on a timescale that enables observation of the migration and transition of the bedforms.

Therefore, the experimentally observed processes of open channel flow are here compared to the turbidite deposits (as was also previously done by, for example, Postma et al. 2014). However, the authors do acknowledge that the turbidity current and open channel flow regimes may not be completely consistent, such as suggested by the Fedele et al. (2016) experiments where supercritical density flow deposits contained ripples and dunes, further adding to the complexity of sedimentary structures formed by supercritical flows.

Comparison to coarse sediment transport in modern channels

Some modern sea floor bedforms documented in submarine channels, and interpreted as of Froude supercritical flow origin, have been shown to migrate less than one bedform wavelength per flow event (Smith et al., 2007; Conway et al., 2012; Normandeau et al. 2014; Hizzett et al., 2017). This intermittent, and thus slow, migration of the bedforms and the experimental observations that coarse clast are deposited just downstream of the first hydraulic jump seem to imply that most gravel in each scour entered the system during the same event, and that these gravel clusters propagate downstream at a very slow rate of about one bedform-length per event. Such scour confined gravels have been observed in the scour axis, with a discrete change to a sand dominated succession on the bench inside the active conduits of submarine channels (Paull et al., 2010). However, the stepwise migration might only apply during relatively low-density flows, because the recent observations of Paull et al. (2018) have shown that during high-density events clast-like instruments can be transport down the channel for kilometres. The latter may be further corroborated by the fact that the shear stresses in the experimental setting are likely considerably lower than in high-density flow conditions.

Mud deposition from supercritical flow

One of the key outcomes of the here documented experiments is that silt and clay can be deposited at hydraulic jumps, as matrix or layers, without a general waning of the flow or boundary condition changes, expanding the dynamic deposition of mud to supercritical flow conditions. The Juncal Formation and La Jolla Group outcrops also display a variety of fine-grained deposits in scour and fill structures, tens of metres deep, that consist of sandstone to pebbly granule lenses overlain by siltstones and fine sandstones (Ono & Plink Björklund, 2018; Fig. 18A and B). The scour and fill structures occur as erosionally based, multi-scaled (0.1 to 20.0 m deep and a few metres to 30 m wide) scours, in places with basal sandstone or conglomerate lenses, 0.1 to 0.3 m (up to 2.0 m) thick and 10 to 20 m wide, and dominated by convex-up low angle laminations and scour and fill structures. These scour and fill structures are similar to the multi-scaled scour and fill structures produced by experiments, where coarser deposits occur along basal broad scour surfaces and are overlain by considerably finer grained deposits composed of fine-grained sand, silt and clay. (Figs 13 and 18C).

CONCLUSIONS

In contrast to previous experiments this study shows that cyclic steps can produce more complex laminations and sedimentary structures than consistent backsets, including undulating planar to upstream and downstream dipping laminae. These experiments indicate that these sedimentary structures are strongly controlled by the transient hydraulic jump size, stability and migration rate, suspension transport and grain-size calibre, and the substrate cohesion. Larger hydraulic jumps tend to form more variable sedimentary structures than smaller hydraulic jumps which mostly form undulating laminations. Stable migration of large hydraulic jumps forms flat erosion surfaces and consistent backsets, and unstable migration forms uneven scours and different erosionally bound 'scour and fill' structures. Gravels in these conditions are deposited as lenses and mounds. Passage of multiple hydraulic jumps erodes previous bedforms partially or completely and re-deposits the sediments at or downstream of the jump. Gravels are deposited at the very edge of the hydraulic jump and sands further downstream due to differences in their settling velocity. This segregation produces downstream fining in some gravelly bedforms, as well as upward fining with upstream migration of the hydraulic jump. Cohesive substrates induce loading and sliding of gravels into the scour centre, producing low-angle gravel lenses overlain with finer-grained deposits. These gravel lenses encased in finer-grained deposits display a heterolithic appearance. This resultant lateral and vertical grain-size variability in the sedimentary structures is consistent with the fact that similar structures in the outcrops are formed by the cyclic step migration rather than changes in overall flow conditions.

ACKNOWLEDGEMENTS

This work was funded by INPEX Corporation and the RioMAR Consortium (BHP Billiton, Chevron, Devon, Eni, ExxonMobil, Petrom, Shell, Statoil, Wintershall and Woodside). Thony van der Gon-Netscher is acknowledged for technical support in the Eurotank Flume Laboratory, which made this work possible. Regarding the grain-size analysis, João Alexandre is thanked for the technical discussion and Coen Mulder is thanked for the technical assistance. M.J.B. Cartigny is funded through a Royal Society Research Fellowship. We also thank Sedimentology reviewers Jörg Lang, Jean Francois Ghienne, and the Associate Editor Alexandre Normandeau for constructive comments.

REFERENCES

Abdullatif, O.M., 1989. Channel-fill and sheet-flood facies sequence in the ephemeral terminal River Gash, Kassala, Sudan. Sed. Geol., 63, 171–184.

Allen, J.R.L. (1982) Sedimentary Structures: Their Character and Physical Basis1, Elsevier, Amsterdam.

Alexander, J., Bridge, J.S., Cheel, R.J. and Leclair, S.F. (2001) Bedforms and associated sedimentary structures formed under water flows over aggrading sand beds. Sedimentology, 48, 133–152.

Baas, J.H., Best, J.L. and Peakall, J (2016) Predicting bedforms and primary current stratification in cohesive mixtures of mud and sand. Journal of the Geological Society 173: 12–45.

Balmforth, N. and Vakil, A. (2012). Cyclic steps and roll waves in shallow water flow over an erodible bed. Journal of Fluid Mechanics, 695, 35-62. doi:10.1017/jfm.2011.555

Billi, P. (2007) Morphology and sediment dynamics of ephemeral stream terminal distributary systems in the Kobo Basin (northern Welo, Ethiopia). Geomorphology 85, 98–113.

Bouma, A.H. (1962) Sedimentology of Some Flysch Deposits: A Graphic Approach to Facies Interpretation. Elsevier, Amsterdam (168 pp.).

Bromley, M.H., 1991. Variations in fluvial style as revealed by architectural elements, Kayenta Formation, Mesa Creek, Colorado, USA: evidence for both ephemeral and perennial fluvial processes. In: Miall, A.D., Tyler, N. (Eds.), The Three-Dimensional Facies Architecture of Terrigenous Clastic Sediments and its Implications for Hydrocarbon Discovery and Recovery. SEPM Concepts in Sedimentology and Palaeontology 3, 94–102.

Cartigny, M.J.B., Ventra, D., Postma, G. and Van Den Berg, J.H. (2014) Morphodynamics and sedimentary structures of bedforms under supercritical-flow conditions: new insights from flume experiments. Sedimentology, 61, 712–748.

Casalbore, D., Romagnoli, C., Bosman, A. and Chiocci, F. L. (2014) Largescale seafloor waveforms on the flanks of insular volcanoes (Aeolian Archipelago, Italy), with inferences about their origin. Mar. Geol. 355, 318–329.

Chow, Ven Te (1959) Open-channel Hydraulics. McGraw-Hill Book, New York.

Clare, M., Le Bas, T., Price, D., Hunt, J., Sear, D., Cartigny, M.J.B., Vellinga, A., Symons, W., W., Firth, C. and Cronin, S. (2018) Complex and cascading triggering of submarine landslides and turbidity currents at volcanic islands revealed from integration of high-resolution onshore and offshore surveys Front. Earth. Sci. 10.3389/feart.2018.00223

Conway, K.W., Barrie, J.V., Picard, K. and Bornhold, B.D. (2012) Submarine channel evolution: active channels in fjords, British Columbia, Canada. Geo-Marine Letters 32, 301–312.

Covault, J.A., Kostic, S., Paull, C.K., Ryan, H.F. and Fildani, A. (2014) Submarine channel initiation, filling and maintenance from sea-floor geomorphology and morphodynamic modelling of cyclic steps. Sedimentology, 61, 1031–1054.

Covault, J.A., Kostic, S., Paull, C.K., Sylvester, Z. and Fildani, A. (2017) Cyclic Steps and related supercritical bedforms: Building blocks of deep-water depositional systems, Western North America. Mar. Geol., 393, 4–20.

Dietrich, P., Ghienne, J.-F., Normandeau, A. and Lajeunesse, P. (2016) Upslope-migrating bedforms in a proglacial sandur delta: cyclic steps from river-derived underflows? J. Sed. Res., 86, 113–123.

Duller, R.A., Mountney, N.P., Russell, A.J. and Cassidy, N.C. (2008) Architectural analysis of a volcaniclastic jökulhlaup deposit, southern Iceland: sedimentary evidence for supercritical flow. Sedimentology, 55, 939–964.

Eggenhuisen, J.T, Cartigny, M.J.B. and J. de Leeuw (2017) Physical theory for near-bed turbulent particle-suspension capacity. Earth Surface Dynamics, 5, 269-281, doi:10.5194/esurf-5-269-2017.

Fagherazzi, S. and Sun, T (2003) Numerical simulations of transportational cyclic steps. Comput. Geosci., 29, 1143–1154.

Fedele and Hoyal (2016) Bedforms created by gravity flows. In: Budd, D., Hajek, E. and Purkis, S. (Eds.), Autogenic Dynamics and Self-Organization in Sedimentary Systems. SEPM, Special Publication 106, 95–121.

Fielding, C.R. (2006) Upper flow regime sheets, lenses and scour fills: extending the range of architectural elements for fluvial sediment bodies. Sed. Geol., 190, 227–240.

Fielding, C.R., Alexander, J. and Allen, J. (2017) The role of discharge variability in the formation and preservation of alluvial sediment bodies. Sed. Geol., 365. 1–20.

Fielding, C.R., Allen, J.P., Alexander, J. and Gibling, M.R. (2009) A facies model for fluvial systems in the seasonal tropics and subtropics. Geology 37, 623–626

Fildani, A., Normark, W.R., Kostic, S. and Parker, G. (2006) Channel formation by flow stripping: large-scale scour features along the Monterey East Channel and their relation to sediment waves. Sedimentology, 53, 1265–1287.

Foley, M.G., 1978. Scour and fill in steep, sand-bed ephemeral streams. AAPG Bull., 89, 559–570.

Frostick, L.E. and Reid, I., 1977. The origin of horizontal laminae in ephemeral stream channel fill. Sedimentology 24, 1–10.

Fricke, A.T., Sheets, B.A., Nittrouer, C.A., Allison, M.A. and Ogston, A.S. (2015) An examination of Froude-supercritical flows and cyclic steps on a subaqueous lacustrine delta, Lake Chelan, Washington, U.S.A. J. Sed. Res., 85, 754–767

Gilbert, G.K. (1914) The transportation of debris by running water. U.S. Geol. Surv. Prof. Pap., 86, 263.

Guy, H. P., Simons, D. B. and Richardson, E. V. (1966) Summary of alluvial channel data from flume experiments 1956–1961. U.S. Geol. Surv. Prof. Paper, 462-I, 96 pp.

Hage, S., Cartigny, M. J. B., Michael, C., Sumner, E. J., Vendettuoli, D., Hughes Clarke, J. E., Hubbard, S., Talling, P. J., Lintern, D. G., Stacey, C., Englert, R., Vardy, M., Hunt, J., Yokokawa, M., Parsons, D., Hizzett, J., Azpiroz, M. and Vellinga, A. (2018). How to recognize crescentic bedforms formed by supercritical turbidity currents in the geologic record: Insights from active submarine channels. Geology. 46. 563-566.

Hand, B.M. (1974) Supercritical flow in density currents. J. Sed. Res., 44, 637–648.

Hiscott, R. N. (1994). Traction-Carpet Stratification in Turbidites-Fact or Fiction? J. Sed. Res., 64A. 204–208

Hizzett, J., Hughes Clarke, J. E., Sumner, E. J., Cartigny, M. J. B., Talling, P. J. and Clare, M. (2017). Which Triggers Produce the Most Erosive, Frequent, and Longest Runout Turbidity Currents on Deltas? Geophysical Research Letters. 10.1002/2017GL075751.

Hofstra, M, Peakall, J., Hodgson, D. and Stevenson, C. (2018). Architecture and morphodynamics of subcritical sediment waves in an ancient channel-lobe transition zone. Sedimentology. 65, 2339–2367.

Hughes Clarke, J.E. (2016) First wide-angle view of channelized turbidity currents links migrating cyclic steps to flow characteristics. Nat. Commun., 7. doi: 10.1038/ncomms11896.

Ito, M. (2010) Are coarse-grained sediment waves formed as downstream-migrating antidunes? Insight from an early Pleistocene submarine canyon on the Boso Peninsula, Japan. Sed. Geol., 226, 1–8.

Ito, M., Ishikawa, K. and Nishida, N. (2014) Distinctive erosional and depositional structures formed at a canyon mouth: a lower Pleistocene deep-water succession in the Kazusa forearc basin on the Boso Peninsula, Japan. Sedimentology, 61, 2042–2062.

Ito, M. and Saito, T. (2006) Gravel Waves in an Ancient Canyon: Analogous Features and Formative Processes of Coarse-Grained Bedforms in a Submarine-Fan System, the Lower Pleistocene of the Boso Peninsula, Japan. J. Sed. Res., 76, 1274-1283

Jorritsma, J. (1973) Sluiting tijdelijke toegang Europoort - onderzoek naar de taludhellingen onder water aangebracht zand - verslag model onderzoek: Waterloopkundig Laboratorium.

Kennedy, J.F. (1961) Stationary Waves and Antidunes in Alluvial Channels. W.M. Keck Laboratory of Hydraulics and Water Research, California Institute of Technology, Report KH-R-2, 146 pp.

Komar, P.D. (1971) Hydraulic jumps in turbidity currents. Geol. Soc. Am. Bull., 82, 1477–1487.

Kostic, S. and Parker, G. (2006) The response of turbidity currents to a canyon-fan transition: Hydraulic jumps and depositional signatures. J. Hydraul. Res., 44, 631–653.

Kubo, Y. and Nakajima, T. (2002). Laboratory experiments and numerical simulation of sediment-wave formation by turbidity currents. Mar. Geol., 192. 105-121.

Lang, J. and Winsemann, J. (2013). Lateral and vertical facies relationships of bedforms deposited by aggrading supercritical flows: from cyclic steps to humpback dunes.
Sed. Geol., 296, 36–54.

Lang, J., Brandes, C. and Winsemann, J. (2017). Erosion and deposition by supercritical density flows during channel avulsion and backfilling: Field examples from coarse-grained deepwater channel-levée complexes (Sandino Forearc Basin, southern Central America). Sed. Geol., 349. 79–102.

Lang, J., Sievers, J., Loewer, M., Igel, J. and Winsemann, J. (2017) 3D architecture of cyclic-step and antidune deposits in glacigenic subaqueous fan and delta settings: Integrating outcrop and ground-penetrating radar data. Sed. Geol., 362, 83-100

Lowe, D.R. (1982) Sedimentary gravity flows: II. Depositional models with special reference to the deposits of high-density turbidity currents. J. Sed. Petrol., 52, 279–297.

Lüdmann, T., C. Betzler, G.P. Eberlib, J. Reolid, J.J.G. Reijmer, C.G. Sloss, O.M. Bialik, C.A. Alvarez-Zarikian, M. Alonso-Garcí, C.L. Blättler, J.A. Guo, S. Haffen, S. Horozal, M. Inoue, L. Jovane, D. Kroon, L. Lanci, J.C. Laya, A.L.M. Mee, M. Nakakuni, B.N. Nath, K. Niino, L.P. Petruny, S.D. Pratiwi, A.L. Slagle, X. Su, P.K. Swart, J.D. Wright, Z. Yao and J.R. Young, 2018, Carbonate Delta Drift: A New Sediment Drift Type: Mar. Geol. , 401, 98-111.

McKee, E.D., Crosby, E.J. and Berryhill, M.L., 1967. Flood deposits, Bijou Creek, Colorado. June 1965. J. Sed. Petrol., 37, 829–851.

Massari, F. (1984) Resedimented conglomerates of a Miocene fandelta complex, Southern Alps, Italy. In: Sedimentology of Gravels and Conglomerates (Eds E.H. Koster, R.J. Steel), Can. Soc. Petrol. Geol. Mem., 10, 259–278.

Massari, F. (1996) Upper-flow-regime stratification types on steep-face, coarse-grained, Gilbert-type progradational wedges. J. Sed. Res., 66, 364–375.

Massari, F. and Chiocci, F. (2006). Biocalcarenite and mixed cool-water prograding bodies of the Mediterranean Pliocene and Pleistocene: Architecture, depositional setting and forcing factors. Geological Society, London, Special Publications. 255. 95-120. 10.1144/GSL.SP.2006.255.01.08.

Mastbergen, D.R. and Winterwerp, J.C. (1987) Het gedrag van zand-watermengselstromingen boven water: Verslag experimentele vervolg studie. Report Z46-02, Delft Hydraulics, Delft, The Netherlands.

Migeon, S., Savoye, B. and Faugeres, J.C. (2000) Quaternary development of migrating sediment waves in the Var deep-sea fan: distribution, growth pattern, and implication for levee evolution. Sed. Geol., 133, 265–293.

Mutti, E. (1992) Turbidite sandstones. Università di Parma, Istituto di Geologia, Agip, Parma, Italy (275 pp.).

Mutti, E., R. Tinterri, G. Benevelli, D. DiBiase and G. Cavanna, 2003, Deltaic, mixed and turbidite sedimentation of ancient foreland basins, in E. Mutti, G.S. Steffens, C. Pirmez, M. Orlando and D. Roberts (eds.), Turbidites; models and problems: Mar. Petrol. Geol., v. 20/6-8, p. 733-755.

Nakajima, T. and Satoh, M. (2001) The formation of large mudwaves by turbidity currents on the levees of the Toyama deep-sea channel, Japan Sea. Sedimentology, 48, 435–463.

Normandeau, A., Dietrich, P., Clarke, J. H., Van Wychen, W., Lajeunesse, P., Burgess, D. and Ghienne, J. (2018). The retreat pattern of glaciers controls the occurrence of turbidity currents on high-latitude fjord deltas. EarthArXiv. https://doi.org/10.31223/osf.io/djfny.

Normandeau, A., Lajeunesse, P., St-Onge, G., Bourgault, D., St-Onge-Drouin, G., Senneville, S. and Belanger, S. (2014) Morphodynamics in sediment-starved inner-shelf submarine canyons (Lower St. Lawrence Estuary, Eastern Canada). Mar. Geol., 357, 243–255.

Normark, W.R., Piper, D.J.W., Posamentier, H., Pirmez, C. and Migeon, S. (2002) Variability in form and growth of sediment waves on turbidite channel levees. Mar. Geol., 192, 23–58.

North, C.P. and Taylor, K.S. (1996) Ephemeral–fluvial deposits: integrated outcrop and simulation studies reveal complexity. AAPG Bulletin 80, 811–830.

Ono, K. and Plink-Björklund, P., 2018, Froude supercritical flow bedforms in deepwater slope channels? Field examples in conglomerates, sandstones and fine-grained deposits. Sedimentology, v. 48, p.133–31, doi: 10.1111/sed.12396.

Owen, G. (2003) Load structures: gravity-driven sediment mobilization in the shallow subsurface. From: VAN RENSBERGEN, R, HILLIS, R.R., MALTMAN, A.J. & MORLEY, C.K. (eds) 2003. Subsurface Sediment Mobilization. Geological Society, London, Special Publications, 216, 21-34.

Paull, C. K., Talling, P. J., Maier, K., Parsons, D., Xu, J., Caress, D., Gwiazda, R., Lundsten, E. M., Anderson, K., Barry, J. P., Chaffey, M., O'reilly, T., Rosenberger, K., Gales, J. A., Kieft, B., McGann, M., McCann, M., Sumner, E. J. Clare, M. and Simmons, S.(2018). Powerful turbidity currents driven by dense basal layers. Nature Communications. 9. 10.1038/s41467-018-06254-6.

Paull, C.K., UsslerIII, W., Caress, D.W., Lundsten, E., Covault, J.A., Maier, K.L., Xu, J. and Augenstein, S. (2010) Origins of large crescent-shaped bedforms within the axial channel of Monterey Canyon, offshore California. Geosphere, 6, 755–774.

Plink-Björklund, P. (2015) Morphodynamics of rivers strongly affected by monsoon precipitation: review of depositional style and forcing factors. Sed. Geol., 323, 110–147.

Plink-Björklund, P. (2018) Latitudinal Controls on River Systems: Implications of Precipitation Variability, in Latitudinal Controls on Stratigraphic Models and Sedimentary Concepts, Fraticelli (ed.). SEPM Special Publication 108. DOI: 108. 10.2110/sepmsp.108.05.

Pope, E. L., Jutzeler, M., Cartigny, M. J. B., Shreeve, J., Talling, P. J. and Wright, I. C. (2018). Origin of spectacular fields of submarine sediment waves around volcanic islands. Earth Planet. Sci. Lett. 493, 12–24.

Postma, G. and Cartigny, M.J.B. (2014) Supercritical and subcritical turbidity currents and their deposits – a synthesis. Geology, 42, 987–990.

Postma, G., Cartigny, M.J.B. and Kleverlaan, K. (2009) Structureless, coarse-tail graded Bouma Ta formed by internal hydraulic jump of the turbidity current? Sed. Geol., 219,1 –6.

Postma, G. and Kleverlaan, K. (2018) Supercritical flows and their control on the architecture and facies of small-radius sand-rich fan lobes. Sed. Geol., 364, 53-70.

Postma, G., Kleverlaan, K. and Cartigny, M.J.B. (2014) Recognition of cyclic steps in sandy and gravelly turbidite sequences, and consequences for the Bouma facies model. Sedimentology, 61, 2268–2290.

Postma, G., Hoyal, D.C.J.D., Abreu, V., Cartigny, M.J.B., Demko, T., Fedele, J.J., Kleverlaan, K. and Pederson, K.H. (2016) Morphodynamics of supercritical turbidity currents in the channel-lobe transition zone. In: Submarine Mass Movements and their Consequences (Eds G. Lamarche, J. Mountjoy, S. Bull, T. Hubble, S. Krastel, E. Lane, A. Micallef, L. Moscardelli, C. Mueller, I. Pecher and S. Woelz), Advances in Natural and Technological Hazards Research, 41, 469–478.

Russell, H.A.J. and Arnott, R.W.C. (2003) Hydraulic jump and hyperconcentrated-flow deposits of a glacigenic subaqueous fan: Oak Ridges Moraine, Southern Ontario, Canada. J. Sed. Res., 73, 887–905.

Schmincke, H.-U., Fisher, R. V. and Water, A. C. (1973) Antidune and chute and pool structures in the base surge deposits of the Laacher See area, Germany. Sedimentology, 20. 553–574,

Simons, D. B. and Richardson, E. V. (1961) Forms of bed roughness in alluvial channels. ASCE Proceedings 87(HY3):87–105.

Slootman, A., De Boer, P., Cartigny, M.J.B., Samankassou, E and Moscariello, A. (2019). Evolution of a carbonate delta generated by gateway‐funnelling of episodic currents. Sedimentology. 10.1111/sed.12585.

Smith, D.P., Kvitek, R., Iampietro, P.J. and Wong, K. (2007) Twenty-nine months of geomorphic change in upper Monterey Canyon (2002–2005). Mar. Geol., 236, 79–94.

Stear, W.M., 1985. Comparison of the bedform distribution and dynamics of modern and ancient sandy ephemeral flood deposits in the southwestern Karoo region, South Africa. Sed. Geol., 45, 209–230.

Sohn, Y.K., 1997. On traction-carpet sedimentation. J. Sed. Res., 67,502–509.

Spinewine, B., Sequeiros, O.E., Garcia, M.H., Beaubouef, R.T., Sun, T., Svoye, B. and Parker, G. (2009) Experiments on wedge-shaped deep sea sedimentary deposits inminibasins and/or on channel levees emplaced by turbidity currents. Part II. Morphodynamic evolution of the wedge and of the associated bedforms. J. Sed. Res., 79, 608–628.

Sumner, E.J., Talling, P.J., Amy, L.A., Wynn, R.B., Stevenson, C.J. and Frenz, M. (2012) Facies architecture of individual basin-plain turbidites:
Comparison with existing models and implications for flow processes. Sedimentology, 59, 1850–1887.

Symons, W.O., Sumner, E.J., Talling, P.J., Cartigny, M.J.B. and Clare, M.A. (2016) Large-scale sediment waves and scours on the modern seafloor and their implications for the prevalence of supercritical flows. Mar. Geol., 371, 130–148.

Symons, W.O., Sumner, E.J., Paull, C. K., Cartigny, M.J.B., Xu, J.P., Maier, K. M., Lorenson, T.D. and Talling, P. J. (2017) A new model for turbidity current behavior based on integration of flow monitoring and precision coring in a submarine canyon. Geology, 45, 367–370.

Talling, P.J., Masson, D.G., Sumner, E.J. and Malgesini, G. (2012) Subaqueous sediment density flows: depositional processes and deposit types. Sedimentology, 59, 1937–2003.

Tunbridge, I.P., 1981. Sandy high-energy flood sedimentation—some criteria for recognition, with an example from the Devonian of S.W. England. Sed. Geol., 28, 79–95.

Walker, R.G. (1967) Upper-Fow regime bed forms in turbidites of the Hatch Formation, Devonian of New York State. J. Sed. Petrol., 37, 1052–1058.

Wang, J. and Plink-Björklund, P. (2019) Stratigraphic complexity in fluvial fans: Lower Eocene Green River Formation, Uinta Basin, USA. Basin Research, 10.1111/bre.12350.

Williams, G.E., 1971. Flood deposits of sand-bed ephemeral streams of Central Australia. Sedimentology 17, 1–40.

Winterwerp, J.C., Bakker, W.T., Mastbergen, D.R. and Van Rossum, H. (1992) Hyperconcentrated sand-water mixture flows over erodible bed. J. Hydraul. Engin., 118, 1508–1525.

Yokokawa, M., Okuno, K., Nakamura, A., Muto, T., Miyata, Y. and Naruse, H. (2009) Aggradational cyclic steps: Sedimentary structures found in flume experiments. Proceedings 33rd IAHR Congress, Vancouver, pp. 5547–5554.

Yokokawa, M., Hasegawa, K., Kanbayashi, S. and Endo, N. (2010) Formative conditions and sedimentary structures of sandy 3D antidunes: An application of the gravel step−poolmodel to fine-grained sand in an experimental flume. Earth Surf. Proc. Landf., 35, 1720–1729

Velinga, A.J., Cartigny, M.J.B., Eggenhuisen, J.T. and Hansen, E.W.M. (2017) Morphodynamics and depositional signature of low-aggradation cyclic steps: New insights from a depth-resolved numerical model. Sedimentology, 65, 540-560.

Ventra, D., Cartigny, M.J.B., Bijkerk, J.F. and Acikalin, S. (2015) Supercritical-flow structures on a Late Carboniferous delta front: sedimentologic and paleoclimatic significance. Geology 43, 731–734.

Zellman, K. L., Plink-Bjorklund, P. and Fricke, H. C. (submitted). Testing hypotheses on precipitation variability signatures in the river and floodplain deposits of the Paleogene San Juan Basin, New Mexico, USA. J. Sed. Res.

Fig. 1 (A) Diagram of the experimental flume, Eurotank, Utrecht University, Netherlands. (B) Photograph of the flume, where the main observation panel 6 is shown by a red outline.

Fig. 2. Experiment grain-size distribution. In different runs medium to coarse sand, gravel, silt and clay were added to the original fine-grained sand (see also Table 1): vf – very fine; f – fine; m – medium; c – coarse; vc – very coarse; S – sand; G – gravel.

Fig. 3. Summary of experimental runs with different grain sizes. Laminations are not visible in run 2 due to the very uniform grain size (fine sand). Run 4 produced visible laminations due to the added medium and coarse sand (m-c sand). Run 5 produced even clearer laminations as gravel was added. Adding silt in runs 6 to 9 and kaolin in runs 10 and 11 produced subtle laminations and soft sediment deformation, unless coarse sediment was added also (runs 9 and 11). This paper focuses on runs 5, 9 and 11.

Fig. 4. Froude number time series (left) and distributions (right) at a fixed position from the reference run 2 (A) as compared to runs 5 (B), 9 (C) and 11 (D), measured at a fixed position at the upstream end of panel 6.

Fig. 5. (A) The upstream panels 3, 4 and 5 of run 5 with fine sand, medium to coarse sand and gravel, 48 minutes after the start of feeding coarse sediment. (B) Close-up of panel 4 showing four types of gravel lenses: mound-shaped, wedge-shaped and amalgamated lens-shaped structures, and consistent backset.

Fig. 6. (A) The upstream panels 3 to 5 during run 9 with fine sand, silt, medium–coarse sand and gravel, 33 minutes after start of feeding sediments. (B) Close-up of panel 4. The upper deposit interval is dominated by planar to weakly undulating laminae. There are some loading structures in the centre of the photograph. The lower interval is dominated by larger 'scour and fill' structures. Gravel forms elongated lenses on scour surfaces. (C) Downstream dipping mounded gravelly bedform, forming a sigmoidal shape draping the scour surface in panel 3.

Fig. 7. (A) The main observation panel 6 during run 9, with fine sand, silt, medium to coarse sand and gravel,. (B) Grain size distributions of runs 4, 9 and 11. The samples were taken from the basal 'scour and fill' deposits. (C) Panels 4 and 5 during run 10 display fluidization of the scour surface of the hydraulic jump due to sediment cohesion.

Fig. 8. Comparison large and small hydraulic jumps in run 5, (A) as defined by the water surface difference upstream and downstream of the hydraulic jump related Froude number

upstream and downstream ratio (for example, Fr1/Fr2) and range (for example, Fr1–Fr2), and (B) identified in panel 6. The large hydraulic jump HJ1 has a Froude number ratio of approximately 13 and water depth difference of 18.5 cm, whereas the small hydraulic jump HJ2 has a Froude number ratio of approximately 3 and water depth difference of 2.6 cm.

Fig. 9. Morphodynamics of run 5. (A) Series of photographs of the panel 6: t – duration from the start of the photographic series; T – duration from the start of run, T1 = 3828 s, T2 = 3834 s, T3 = 3852 s, T4 = 3968 s , T5 = 4206 s and T6 = 4244 s. (B) Time lapse sediment surfaces of T = 3968 s from photograph t 4 (A). (C) Mounded gravel bedform close-up image from photograph t4 (A). (D) Consistent backset close-up image from photograph t6 (A). (E) Froude number time series at the upstream end of panel 6. Bedform formation window is shown by a black arrow. A larger hydraulic jump (HJ1) eroded the substrate and was stationary. A smaller hydraulic jump (HJ2) eroded less and migrated quickly. The second larger jump (HJ3) eroded the substrate but migrated at a less stationary rate than HJ1.

Fig. 10. Morphodynamics of run 5. (A) Series of photos of the panel 6: t - duration from the start of the photographic series; T – duration from the start of the run, T1 = 9042 s and T11 = 9080 s. (B) Time lapse sediment surfaces of T = 9144 s. (C) Close-up photograph of amalgamated lenticular gravel bedform from photograph t = 38 s. (D) Froude number time series at the upstream end of panel 6. Bedform formation window is marked by a black arrow.

Fig. 11. Morphodynamics of run 9 with silt. Series of photographs of panel 6 capture the migration of the hydraulic jump downstream (A), within (B) and upstream(C) of panel 6. (D) Close-up of silty laminae formed during the passage of the hydraulic jump in (C).

Fig. 12. Morphodynamics of run 11. (A) Series of photographs of panel 6: t – duration from the start of the photographic series; T – duration from the start of run, T1 = 3066 s, T2 = 3078 s, T3 = 3088s , T4 = 3114 s and T5 = 168 s, T6 = 3450 s , T7 = 3466 s and T8 = 3568 s. (B) Time lapse sediment surfaces from t8 (A) .The time lapse surfaces are not clearly identified in the deposits with uniform grain size. (C) Annotated sedimentary structures from t8 (A). (D) Close-up photograph from t5 (A) shows normally graded gravel-rich lenses and overlain by diffusely laminated fine-grained sands. (E) Snapshot from t3 (A) shows significant upward surge inside the hydraulic jump forming a momentary flame-like structure on the substrate. (F) Froude number time series at the upstream end of panel 6. Bedform formation window is marked by a black arrow.

Fig. 13. Summarized sketches demonstrate the sedimentary structures and bedforms from runs 5 and 11. (A) Sketch from run 5 (Fig. 5). (B) Sketch from run 5 (t6 of Fig. 9A). (C) Sketch from run 11 (t7 of Fig. 12A).

Fig. 14. Time (seconds) versus distance (centimetres) cross-plot of the hydraulic jumps from the downstream end of panel 6 demonstrating how hydraulic jumps move upstream. (A) Plots from runs 2, 5, 9 and 11. (B), (C) and (D) Comparison plots between runs 2 and 5, 2 and 9, and 2 and 11, respectively. Larger markers indicate migration rates of large hydraulic jumps. (E) Example of how the hydraulic jump was traced and the time and the distance are plotted.

Fig. 15. Relationship between migration rate and hydraulic jump trough size.

Fig. 16. Examples of sedimentary structures from gravelly slope channel deposits (see Ono & Plink-Björklund, 2018). (A) Lenticular and amalgamated deposits composed of conglomerate and sandstone exhibiting complex bedsets containing foresets and backsets, Juncal Fomation. (B) Complex wedged shape conglomerates and sandstones, La Jolla Group. (C) Mound shaped conglomerate with foresets and backsets, La Jolla Group. (D) Consistent backsets in conglomerates, La Jolla Group. (E) Normally graded cobble conglomerates that fine upward into sandstone with scour and fill structures, La Jolla Group. (F) Disorganized conglomerate encased by organized conglomerate in a scour fill. (G) A step-like erosion surface filled by foresets of conglomeratic sandstone, Juncal Formation.

Fig. 17. A few to ten metre deep scours in the La Jolla Group.

Fig. 18. Comparison of experimental deposits to fine-grained heterolithic channel deposits of the Juncal Formation (see Ono & Plink-Bjorklund, 2017) to experimental deposits. (A) Scour and fill structures, 0.1 to 2.0 m deep and a few to 10 m wide. (B) Cross-cutting scour and fill structures, a few to 5 m deep and 10 to 30 m wide. (C) Annotated photograph of panel 6 from run 11 (see also Fig. 12) exhibiting multi-scaled scour and fill structures with basal coarse-grained sands: T – duration from the start of run 11.

Table 1. Conditions for individual experimental runs. * *Bold letters show 50th percentile of the flow depth from detailed image analysis (see Cartigny et al., 2014). The other values (0.05 cm) are the initial set depths at the specific location of panel 5. **Volume percentage to the total water volume in the flume.*

Table 2. Summarized process and depositional or erosional response regarding the migration and the size of hydraulic jump and the presence of clay.

Run	Medium grain size (μm)	Duration	Sediment			Discharge type
			Added	In the water of the flume	Out	
1	145	1 hr 57 min	Reference run (only fine-grained sand), no sediment added.			Low
2	145	1 hr 53 min	Reference run (only fine-grained sand), no sediment added.			High
3	145	3 hr 27 min	Coarse sand 50 kg	–	50 kg	Low
4	145	4 hr 46 min	Coarse sand 100 kg	–	100 kg	High
5	145	5 hr 42 min	Coarse sand 50 kg, Gravel 50 kg	–	100 kg	High
6	145	1 hr 46 min	Silt 50 kg (3.4%)**, Coarse sand 25 kg, Gravel 25 kg	*Ca* 3.4% silt	50 kg; and most silt washed out when water was drained	High
7-1	No sampling	1 hr 58 min	Silt 100 kg (6.6%)	*Ca* 6.6% silt	–	Low
7-2	No sampling	32 min	–	*Ca* 6.6% silt	–	High
7-3	No sampling	2 hr 40 min	Silt 50 kg (3.4%)	*Ca* 10.0% silt	–	Low
7-4	No sampling	1 hr 26 min	–	Ca 10.0% silt	–	High
8-1	No sampling	1 hr 54 min	Silt 100 kg (6.6%)	*Ca* 16.5% silt	–	Low
8-2	No sampling	1 hr 49 min	–	*Ca* 16.5% silt	–	High
9	141	4 hr 55 min	Coarse sand 50 kg, Gravel 50 kg	*Ca* 16.5% silt	100 kg; and most silt washed out when water was drained	High
10-1	No sampling	26 min	Kaolin 3kg (0.2%)	*Ca* 0.2% kaolin	–	Low
10-2	No sampling	25 min	–	*Ca* 0.2% kaolin	–	High
10-3	No sampling	56 min	Kaolin 4.5kg (0.3%)	*Ca* 0.5% kaolin	–	High
10-4	No sampling	22 min	–	*Ca* 0.5% kaolin	–	Low
10-5	No sampling	58 min	Kaolin 52.5 kg (3.5%)	*Ca* 4.0% kaolin	–	Low
10-6	No sampling	1 hr 40 min	–	*Ca* 4.0% kaolin	–	High
11	142	6 hr 50 min	Coarse sand 50 kg, Gravel 50 kg	*Ca* 4.0% kaolin	–	High

Average discharge m^3/h	Flow depth (m)*	Flow width (m)	Average flow velocity (m/s)	Froude number (g = 9.8 m/s2)
47	0.05	0.48	0.544	0.78
52	**0.045**	0.48	0.669	**1.01**
49	0.05	0.48	0.567	0.81
52	0.05	0.48	0.602	0.86
53	**0.054**	0.48	0.568	**0.78**
54	0.05	0.48	0.625	0.89
51	0.05	0.48	0.59	0.84
56	0.05	0.48	0.648	0.93
51	0.05	0.48	0.59	0.84
56	0.05	0.48	0.648	0.93
50.5	0.05	0.48	0.584	0.83
53	0.05	0.48	0.613	0.88
51	**0.048**	0.48	0.615	**0.9**
46	0.05	0.48	0.532	0.76
56	0.05	0.48	0.648	0.93
56	0.05	0.48	0.648	0.93
46	0.05	0.48	0.532	0.76
46	0.05	0.48	0.532	0.76
56	0.05	0.48	0.648	0.93
56	**0.061**	0.48	0.531	**0.69**

Process
Unstable migration of large hydraulic jumps
Hydraulic jump migration rate slows
Unstable migration with repeated changes in migration rate
Hydraulic jump scour infilling
Slumping on steep downstream scour face
Deposition downstream of hydraulic jump scour
Stable migration of large hydraulic jumps
Stable migration of hydraulic jump
Hydraulic jump stable scour infilling
Small hydraulic jumps
Hydraulic jump shallow scouring
Presence of clay
Cohesive substrate
Reduced erodibility due to enhanced yield strength
Effect of clay on flow rheology

Depositional or erosional response
Deep scours with steep upstream and downstream faces (Fig. 13A)
Stepwise erosion surfaces with flat and scoured stretches (Fig. 13C)
Steep upstream or downstream dipping strata in scour fill or upward flattening scour fill strata (Fig. 13A) Upward fining basal fills (Fig. 6C)
Structureless or internally deformed gravel lenses (Fig. 13A)
Low-angle long-wavelength planar and convex-up strata with diffuse laminations (Fig.13B)
Flat erosion surface (Fig. 13B)
Consistent backsets (Fig. 13B)
Low-angle undulating laminations (Fig. 13A)
Gravel lenses with deeply loaded base (Fig. 13C)
Shallow stretched scours (Fig. 13C)
Frequent normal grading in basal scour fill (Fig. 13C)

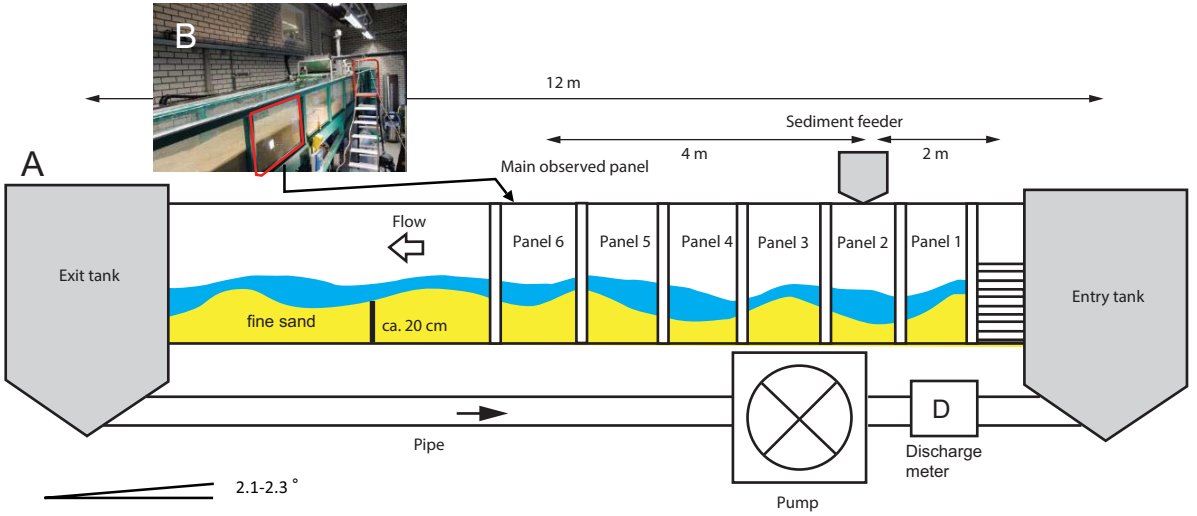
A
B
12 m
Sediment feeder
4 m
2 m
Main observed panel
Flow
Exit tank
Panel 6
Panel 5
Panel 4
Panel 3
Panel 2
Panel 1
Entry tank
fine sand
ca. 20 cm
Pipe
D
Discharge meter
Pump
2.1-2.3 °

Kaolinite clay(D_{50}=3.3)
added in runs 10 and 11.

Silt (D_{50}=31)
added in runs 6, 7, 8 and 9.

Fine sand (D_{50}=146)
used for original
fill of the flume

Medium to coarse sands (D_{50}=428)
added in runs 3, 4, 5, 6, 9 and 11.

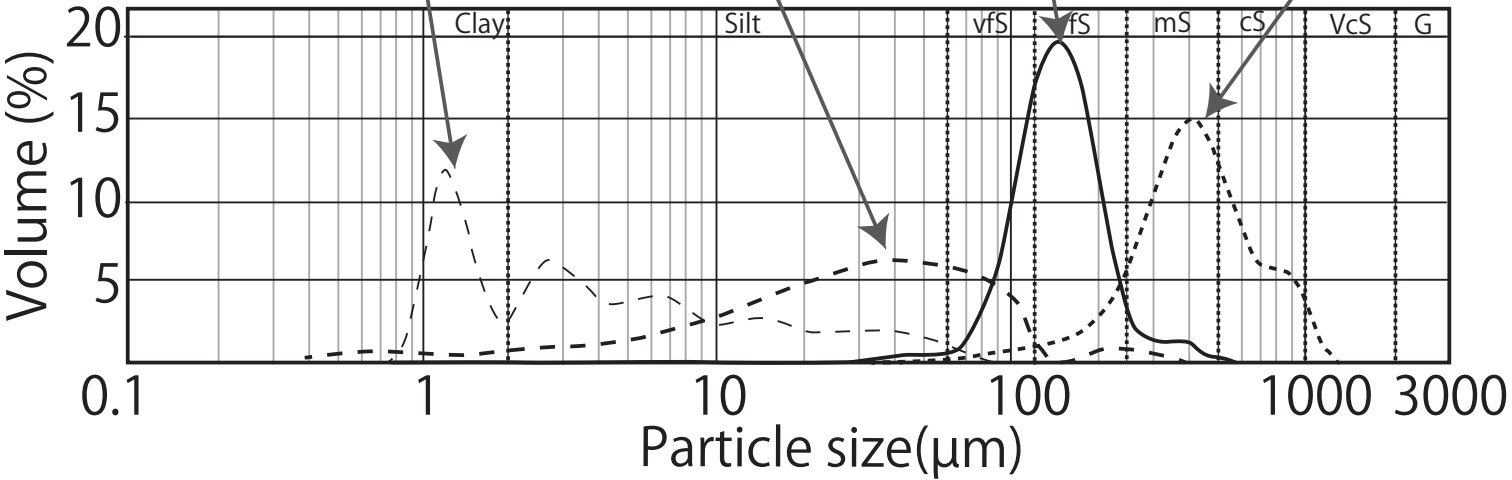

Gravel (2-3mm)
added in runs 5, 6, 9 and 11


Run2
No visible laminations
Run8-2
Weak silty lamination
Run4
Weak sand laminations
Run9
Clear sand to gravel and silt laminations
Loading structure
Silty laminae
Run5
Clear sand to gravel laminations
Run10-6
Subtle laminations
Deposit containing Kaolin
Deposit of pre-run
Run6
Subtle silty sand to gravel laminations
Run11
Clear sand to gravel graded laminations with irregular loading and shallower scours
Run7-4
Subtle silty laminations
Silty laminae

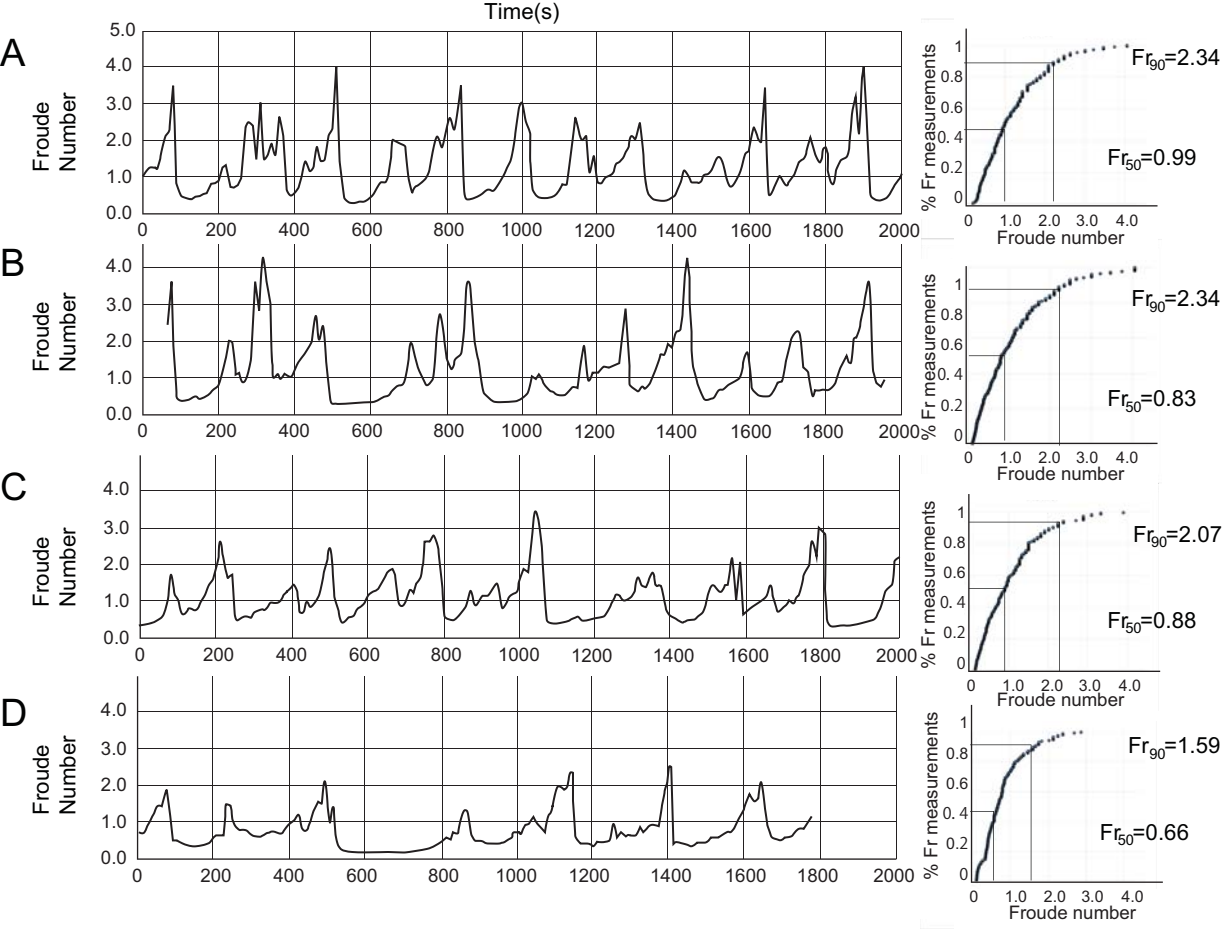
Time(s)
A
B
C
D
Froude Number
% Fr measurements
Froude number
Fr_{90}=2.34
Fr_{50}=0.99
Fr_{90}=2.34
Fr_{50}=0.83
Fr_{90}=2.07
Fr_{50}=0.88
Fr_{90}=1.59
Fr_{50}=0.66

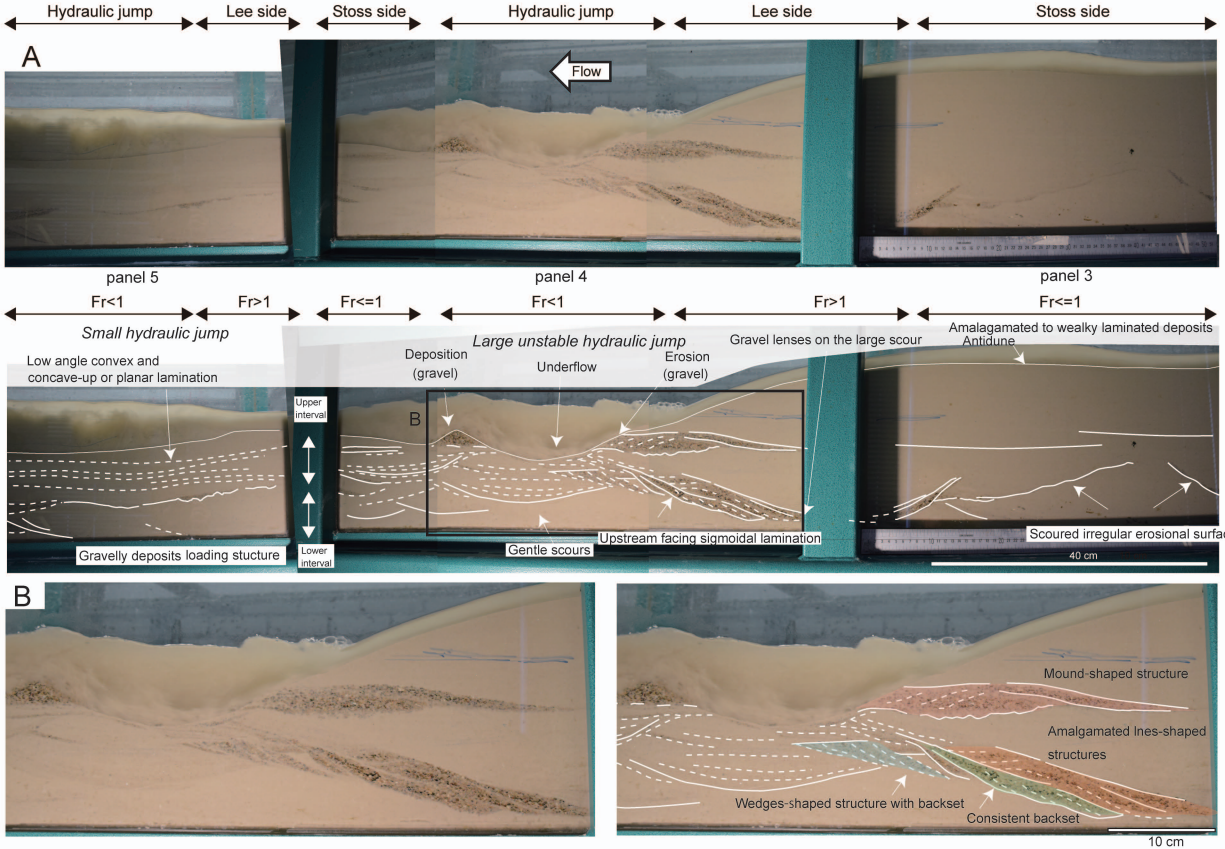
Hydraulic jump
Lee side
Stoss side
Hydraulic jump
Lee side
Stoss side
A
Flow
panel 5
panel 4
panel 3
Fr<1
Fr>1
Fr<=1
Fr<1
Fr>1
Fr<=1
Small hydraulic jump
Low angle convex and concave-up or planar lamination
Gravelly deposits loading stucture
Upper interval
Lower interval
Large unstable hydraulic jump
Deposition (gravel)
Underflow
Erosion (gravel)
B
Gentle scours
Upstream facing sigmoidal lamination
Gravel lenses on the large scour
Amalagamated to wealky laminated deposits
Antidune
Scoured irregular erosional surface
40 cm
B
Mound-shaped structure
Amalgamated lnes-shaped structures
Wedges-shaped structure with backset
Consistent backset
10 cm

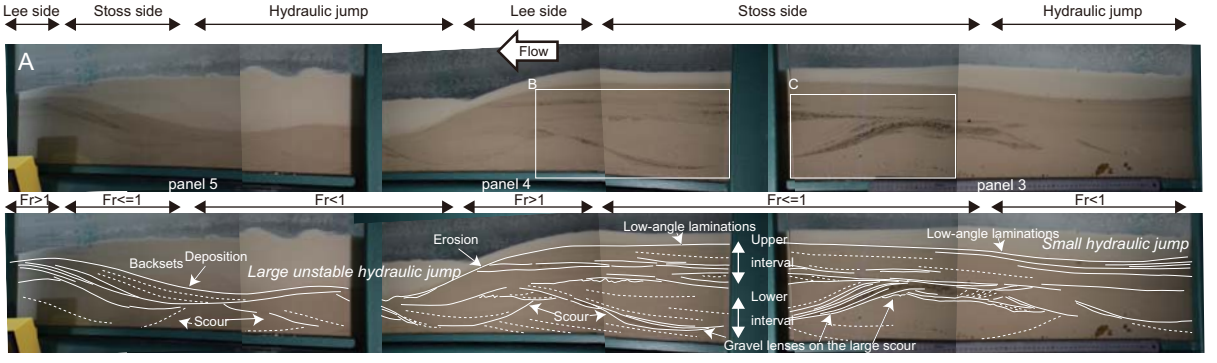
Lee side
Stoss side
Hydraulic jump
Lee side
Stoss side
Hydraulic jump
A
Flow
B
C
panel 5
panel 4
panel 3
Fr>1
Fr<=1
Fr<1
Fr>1
Fr<=1
Fr<1
Backsets
Deposition
Large unstable hydraulic jump
Scour
Erosion
Low-angle laminations
Scour
Upper interval
Lower interval
Low-angle laminations
Small hydraulic jump
Gravel lenses on the large scour

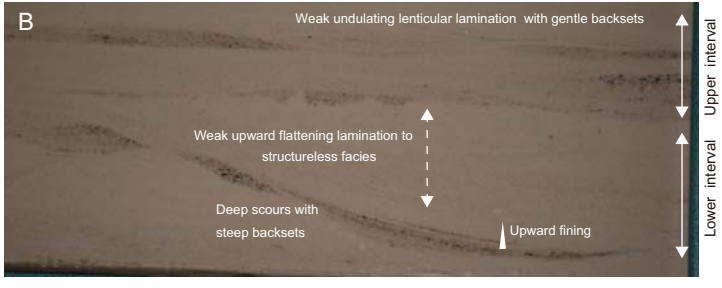
B
Weak undulating lenticular lamination with gentle backsets
Weak upward flattening lamination to structureless facies
Deep scours with steep backsets
Upward fining
Upper interval
Lower interval

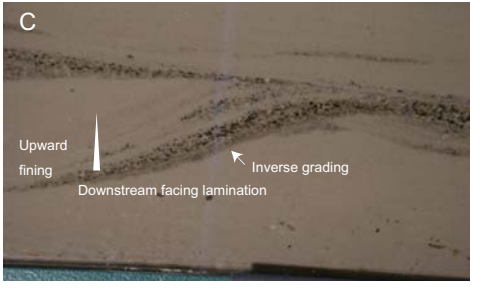
C
Upward fining
Inverse grading
Downstream facing lamination

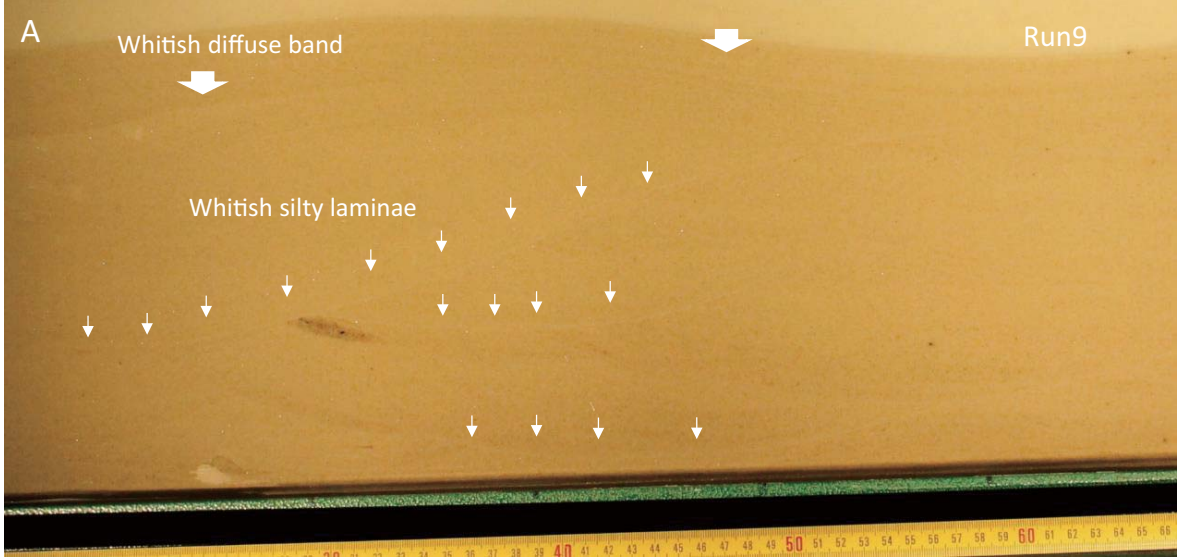
A
Whitish diffuse band
Run9
Whitish silty laminae

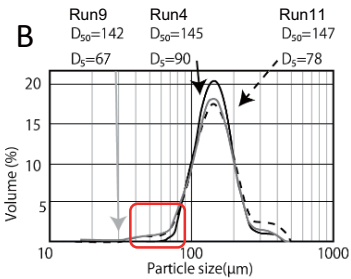
B
Run9
D50=142
D5=67
Run4
D50=145
D5=90
Run11
D50=147
D5=78
20
15
10
5
Volume (%)
10
100
1000
Particle size(μm)

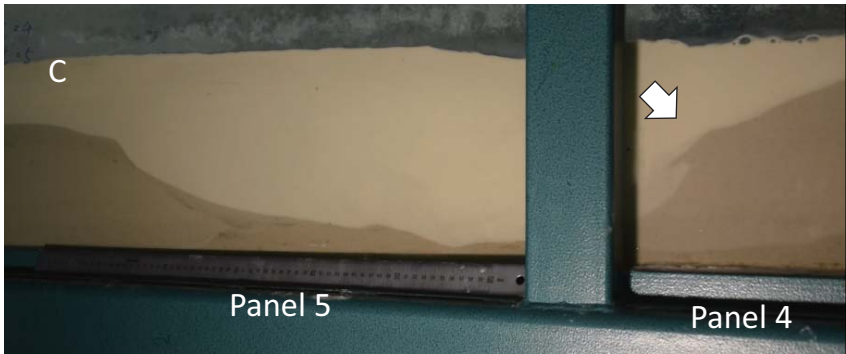
C
Panel 5
Panel 4

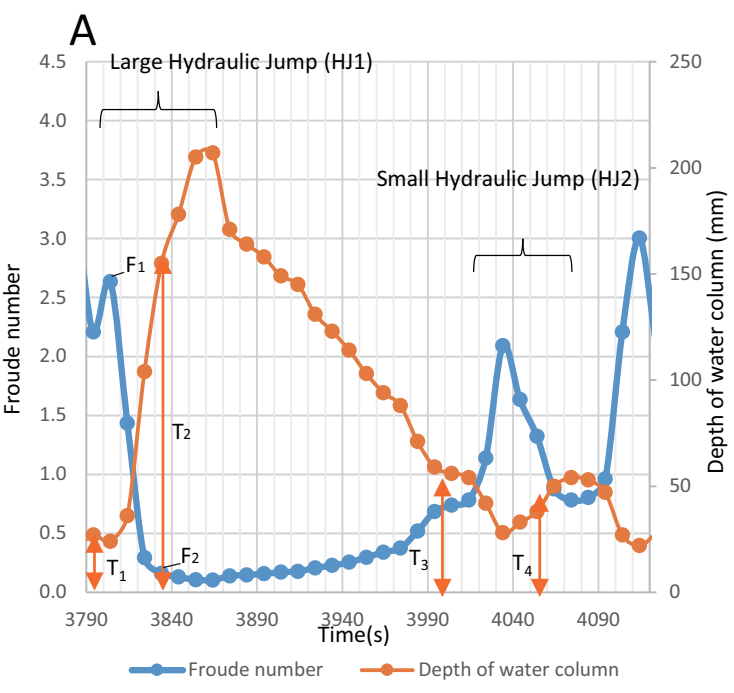
A
Large Hydraulic Jump (HJ1)
Small Hydraulic Jump (HJ2)
F1
F2
T1
T2
T3
T4
Froude number
Depth of water column (mm)
Time(s)
4.5
4.0
3.5
3.0
2.5
2.0
1.5
1.0
0.5
0.0
250
200
150
100
50
0
3790
3840
3890
3940
3990
4040
4090
Froude number
Depth of water column

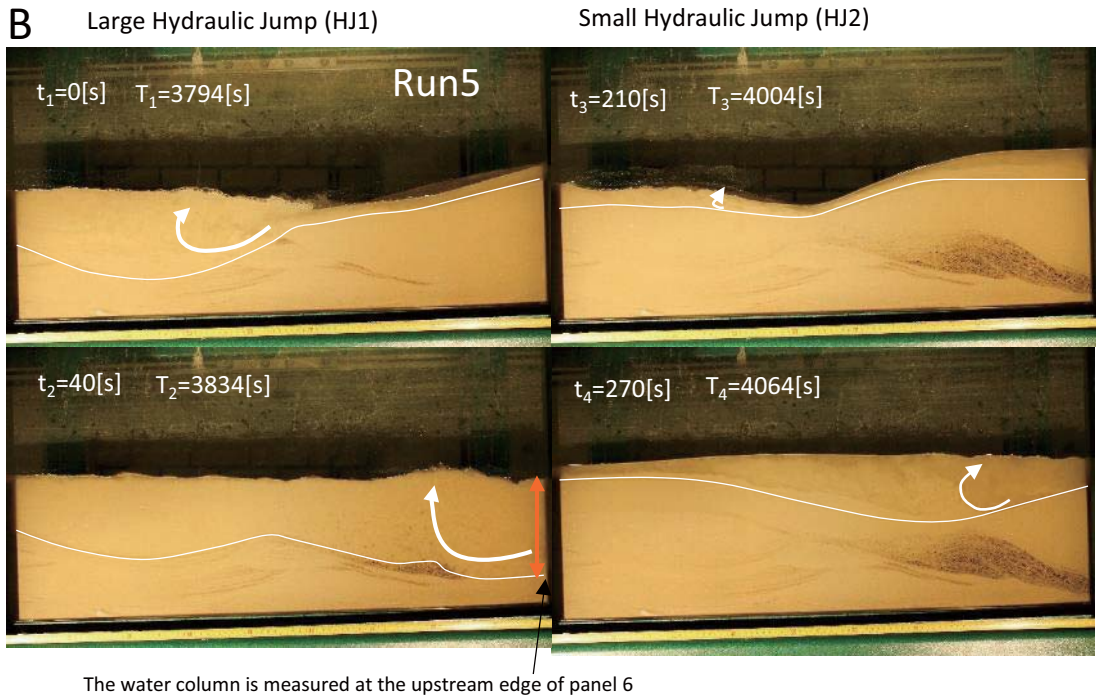
B
Large Hydraulic Jump (HJ1)
Small Hydraulic Jump (HJ2)
Run5
t1=0[s] T1=3794[s]
t3=210[s] T3=4004[s]
t2=40[s] T2=3834[s]
t4=270[s] T4=4064[s]
The water column is measured at the upstream edge of panel 6

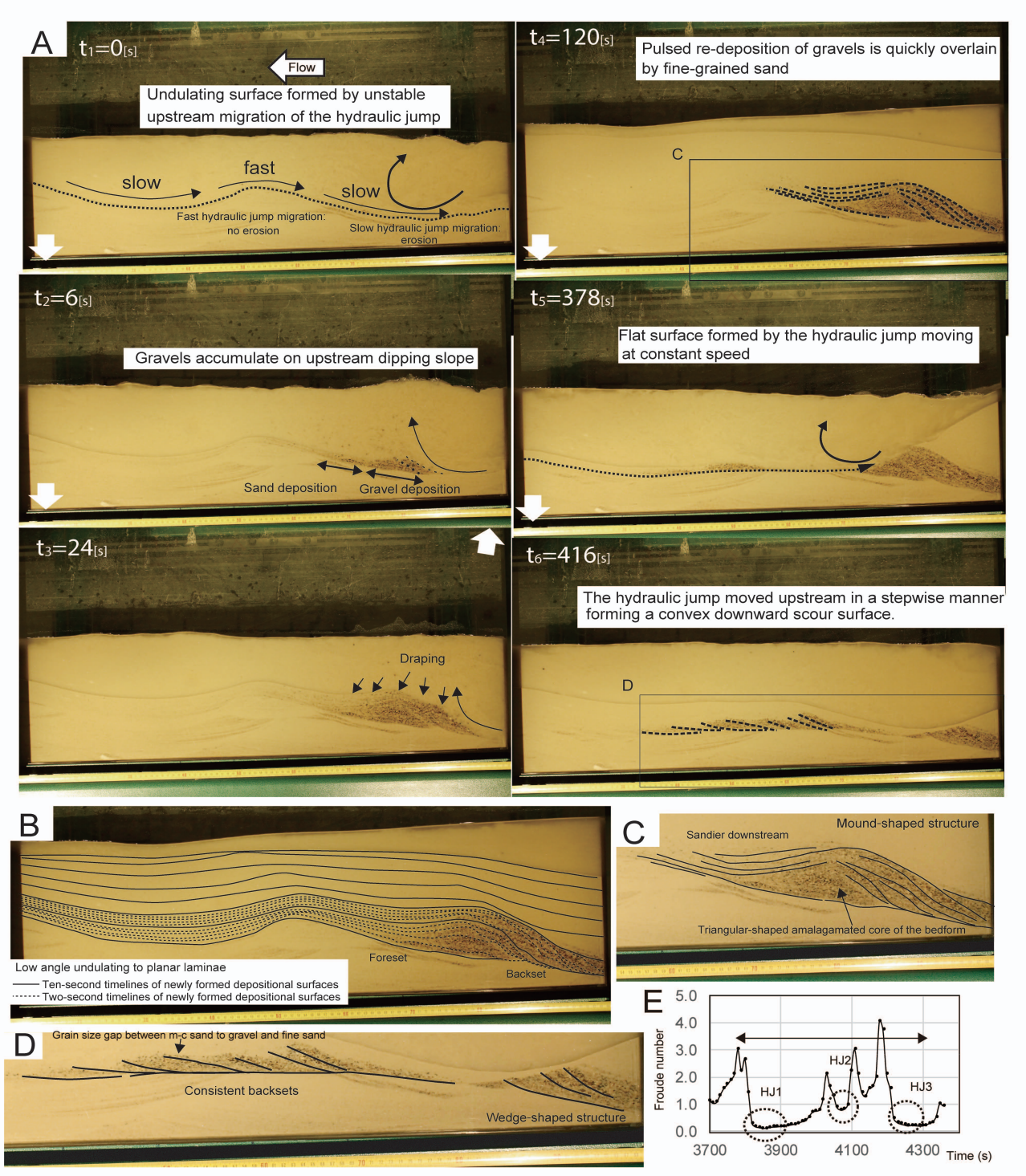
A
t1=0[s]
Flow
Undulating surface formed by unstable upstream migration of the hydraulic jump
slow
fast
slow
Fast hydraulic jump migration: no erosion
Slow hydraulic jump migration: erosion
t2=6[s]
Gravels accumulate on upstream dipping slope
Sand deposition
Gravel deposition
t3=24[s]
Draping
t4=120[s]
Pulsed re-deposition of gravels is quickly overlain by fine-grained sand
C
t5=378[s]
Flat surface formed by the hydraulic jump moving at constant speed
t6=416[s]
The hydraulic jump moved upstream in a stepwise manner forming a convex downward scour surface.
D
B
Foreset
Backset
Low angle undulating to planar laminae
Ten-second timelines of newly formed depositional surfaces
Two-second timelines of newly formed depositional surfaces
C
Sandier downstream
Mound-shaped structure
Triangular-shaped amalagamated core of the bedform
D
Grain size gap between m-c sand to gravel and fine sand
Consistent backsets
Wedge-shaped structure
E
Froude number
5.0
4.0
3.0
2.0
1.0
0.0
HJ1
HJ2
HJ3
3700
3900
4100
4300
Time (s)

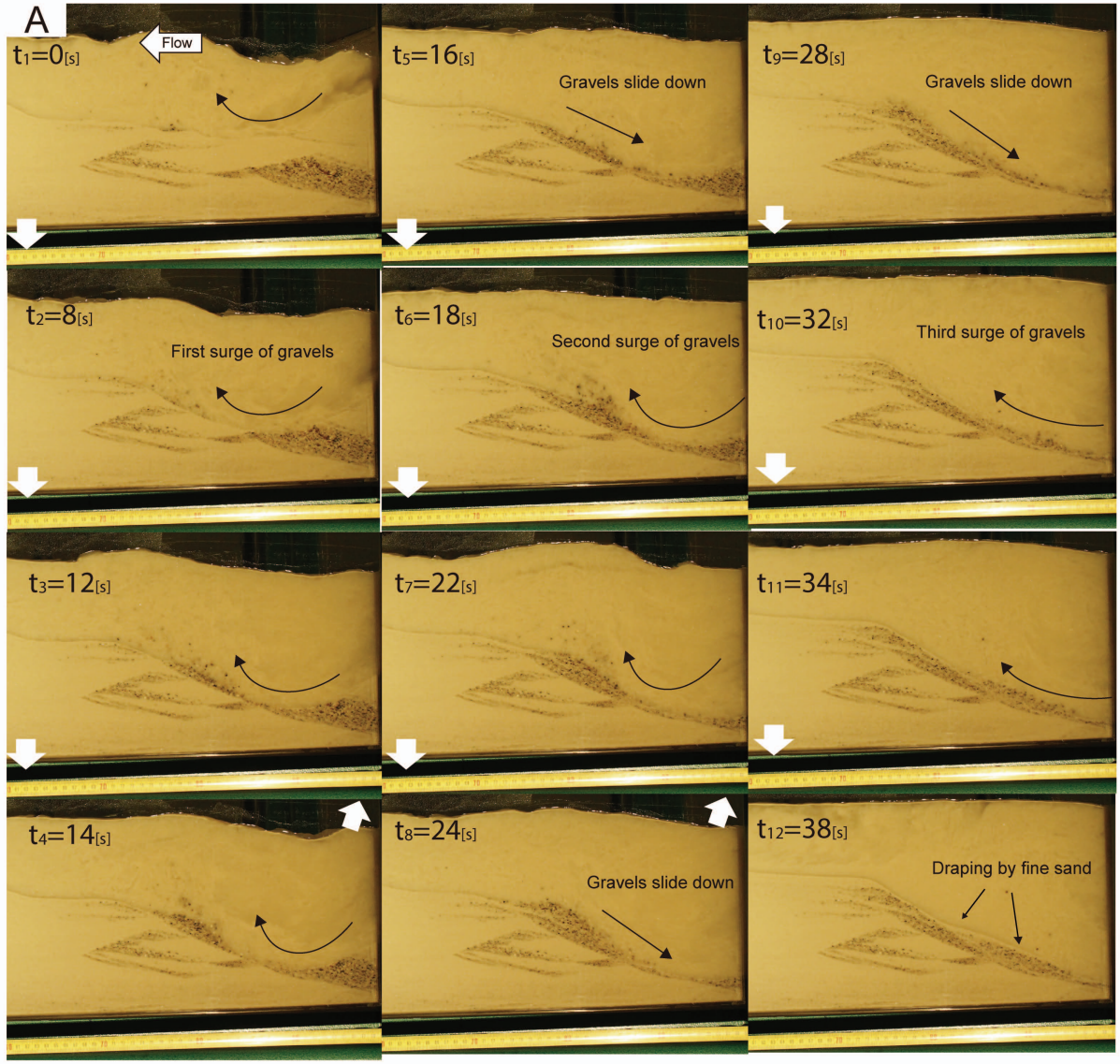
A
Flow
t1=0[s]
t5=16[s]
Gravels slide down
t9=28[s]
Gravels slide down
t2=8[s]
First surge of gravels
t6=18[s]
Second surge of gravels
t10=32[s]
Third surge of gravels
t3=12[s]
t7=22[s]
t11=34[s]
t4=14[s]
t8=24[s]
Gravels slide down
t12=38[s]
Draping by fine sand

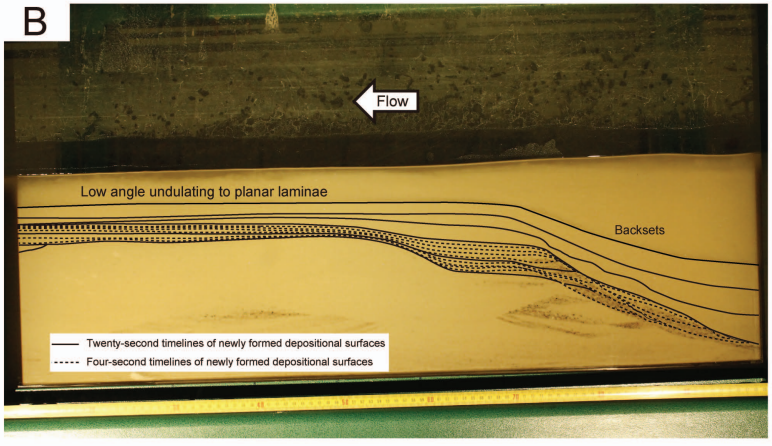
B
Flow
Low angle undulating to planar laminae
Backsets
Twenty-second timelines of newly formed depositional surfaces
Four-second timelines of newly formed depositional surfaces

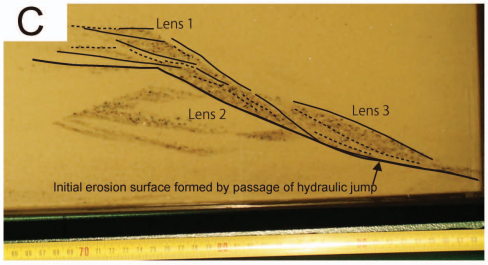
C
Lens 1
Lens 2
Lens 3
Initial erosion surface formed by passage of hydraulic jump

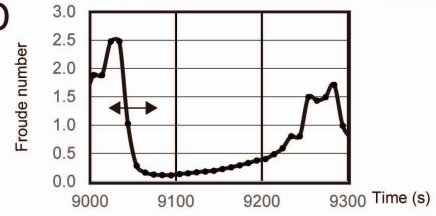
D
Froude number
3.0
2.5
2.0
1.5
1.0
0.5
0.0
9000
9100
9200
9300
Time (s)

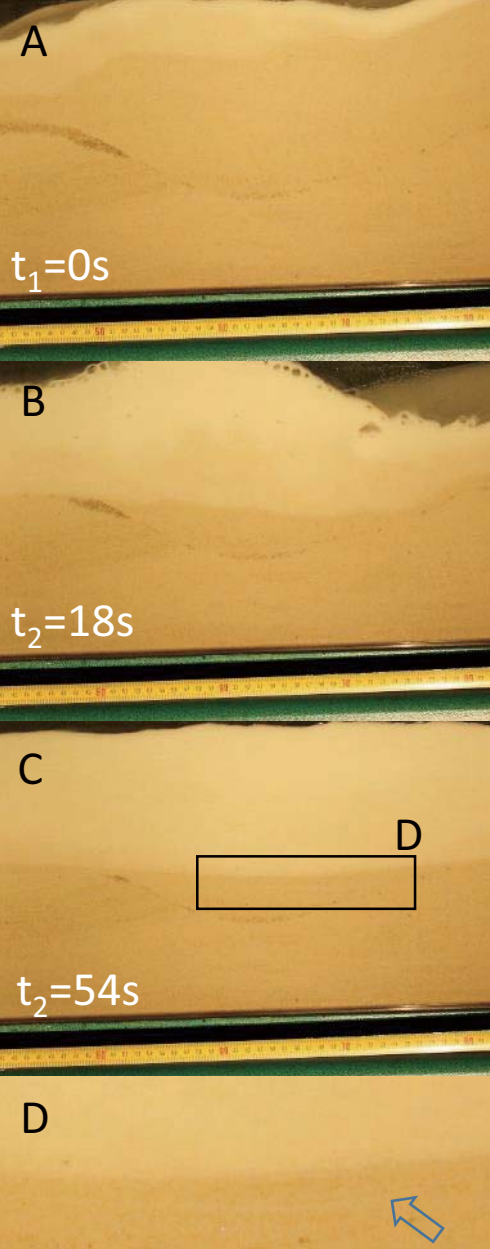
A
t_1=0s
B
t_2=18s
C
D
t_2=54s
D


A
t1=0[s]
Flow
Steep downstream dipping face
t2=12[s]
A relatively shallow scour forms
t3=22[s]
Gravels do not form mounds, loading into substrate, thinly distributed over the surface
Local irregular step-like surface
t4=48[s]
Coarser grains (including gravel) form normal grading
Nomal grading
t5=102[s]
t6=384[s]
Eroded gravels are re-deposited on the edge of the scour
t7=400[s]
Migrating hydraulic jump partially erodes the preceding gravelly lenses, making isolated lenses
Irregular loading structures due to muddy substrates
t8=502[s]

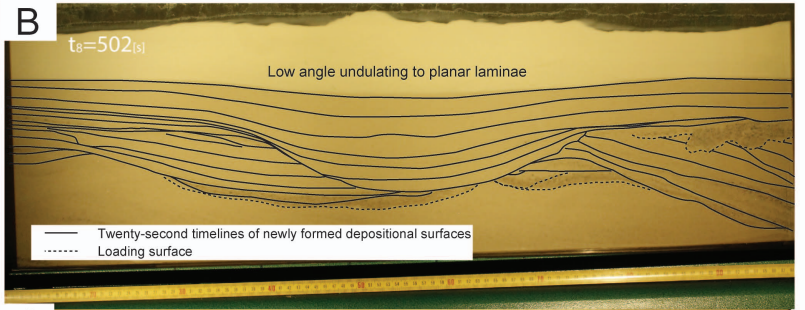
B
t8=502[s]
Low angle undulating to planar laminae
Twenty-second timelines of newly formed depositional surfaces
Loading surface

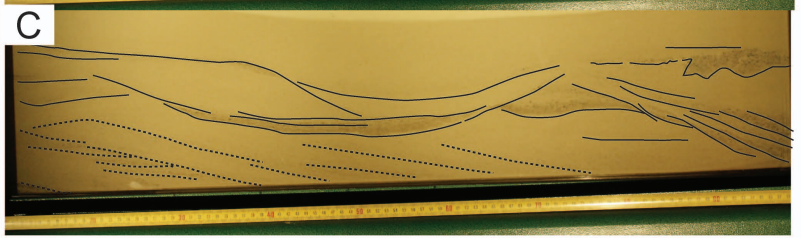
C

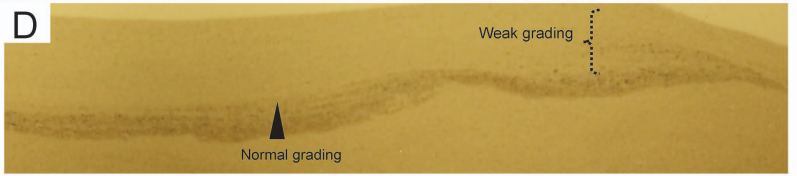
D
Weak grading
Normal grading


E

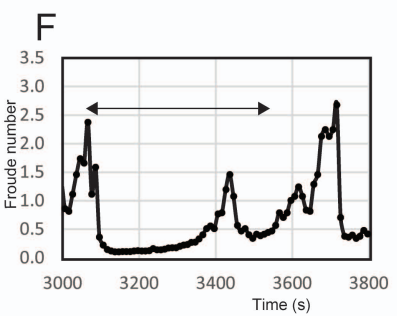
F
Froude number
3.5
3.0
2.5
2.0
1.5
1.0
0.5
0.0
3000
3200
3400
3600
3800
Time (s)

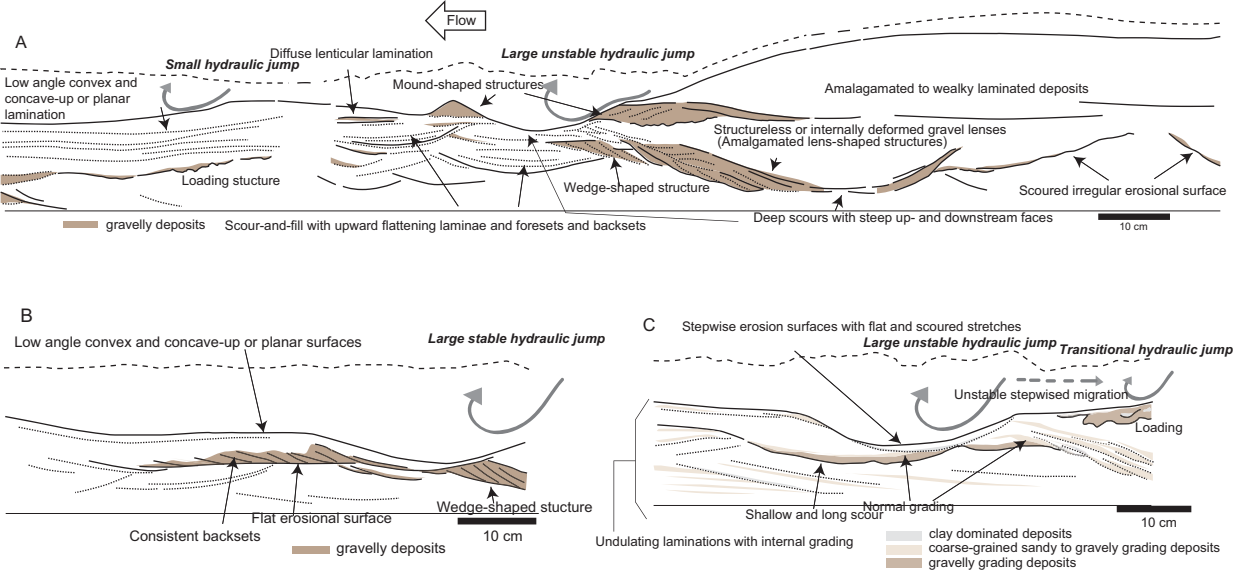
A
Flow
Small hydraulic jump
Diffuse lenticular lamination
Large unstable hydraulic jump
Low angle convex and concave-up or planar lamination
Mound-shaped structures
Amalagamated to wealky laminated deposits
Structureless or internally deformed gravel lenses (Amalgamated lens-shaped structures)
Loading stucture
Wedge-shaped structure
Scoured irregular erosional surface
gravelly deposits
Scour-and-fill with upward flattening laminae and foresets and backsets
Deep scours with steep up- and downstream faces
10 cm
B
Low angle convex and concave-up or planar surfaces
Large stable hydraulic jump
Wedge-shaped stucture
Flat erosional surface
Consistent backsets
gravelly deposits
10 cm
C
Stepwise erosion surfaces with flat and scoured stretches
Large unstable hydraulic jump
Transitional hydraulic jump
Unstable stepwised migration
Loading
Normal grading
Shallow and long scour
10 cm
Undulating laminations with internal grading
clay dominated deposits
coarse-grained sandy to gravely grading deposits
gravelly grading deposits

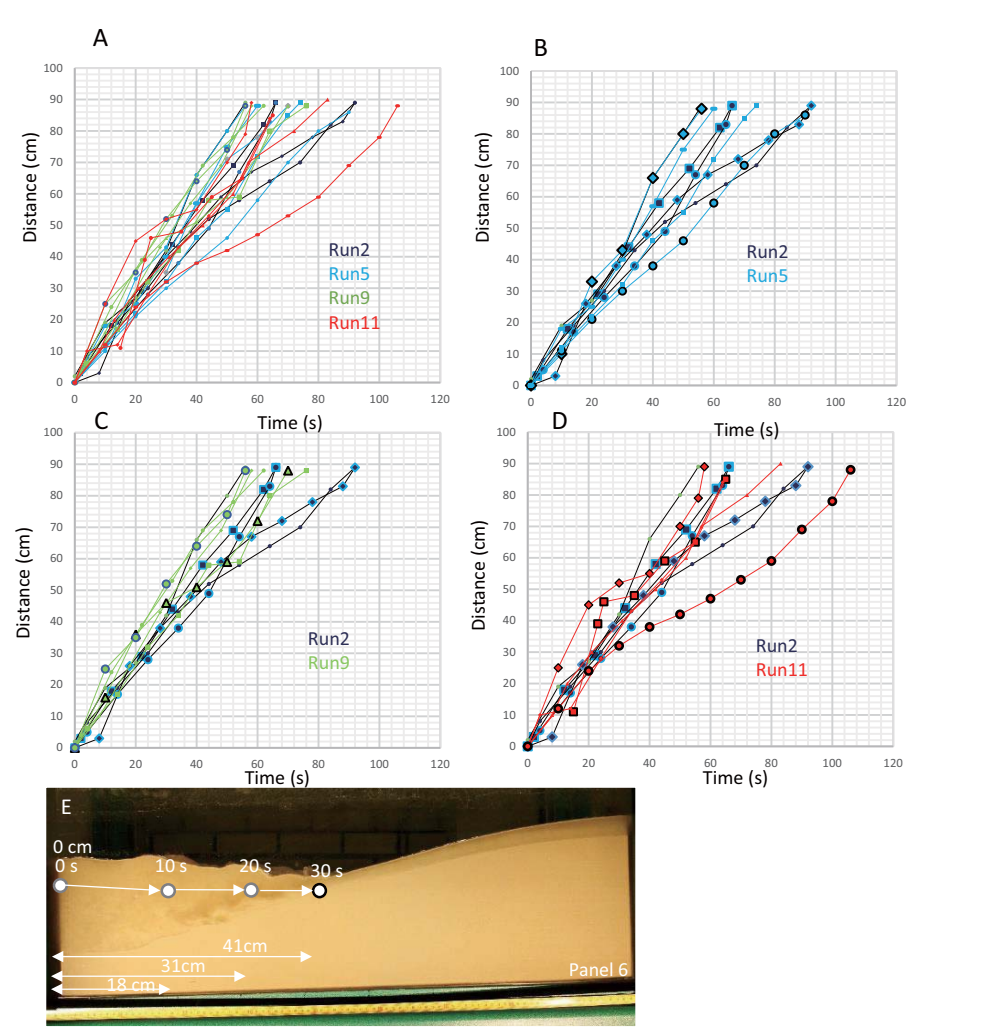
A
Distance (cm)
Time (s)
Run2
Run5
Run9
Run11
B
Distance (cm)
Time (s)
Run2
Run5
C
Distance (cm)
Time (s)
Run2
Run9
D
Distance (cm)
Time (s)
Run2
Run11
E
0 cm
0 s
10 s
20 s
30 s
41cm
31cm
18 cm
Panel 6

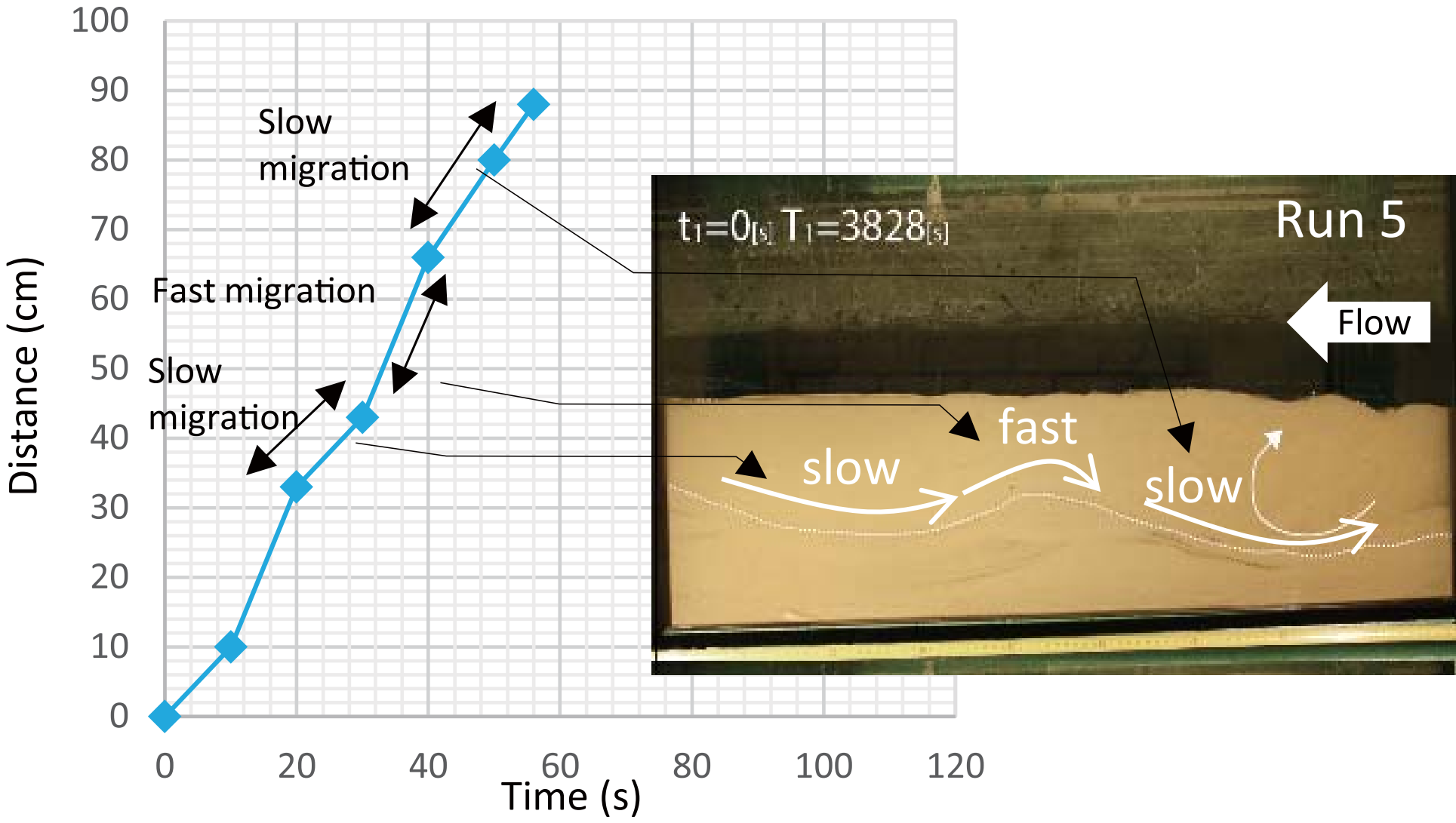
100
90
80
70
60
50
40
30
20
10
0
Distance (cm)
0
20
40
60
80
100
120
Time (s)
Slow
migration
Fast migration
Slow
migration
t1=0[s] T1=3828[s]
Run 5
Flow
fast
slow
slow

Amalgamated erosionally bound gravel lenses with foreset and backet bedding

Wedge-shaped conglomerates and sandstones

Consistent backsets in conglomerates

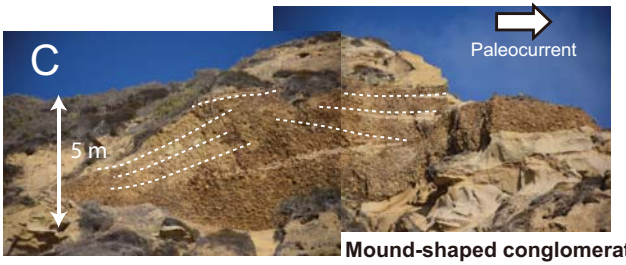

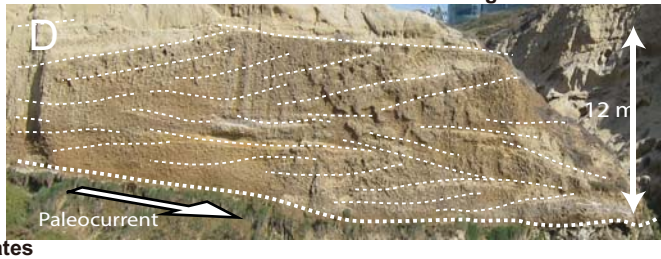

Mound-shaped conglomerates

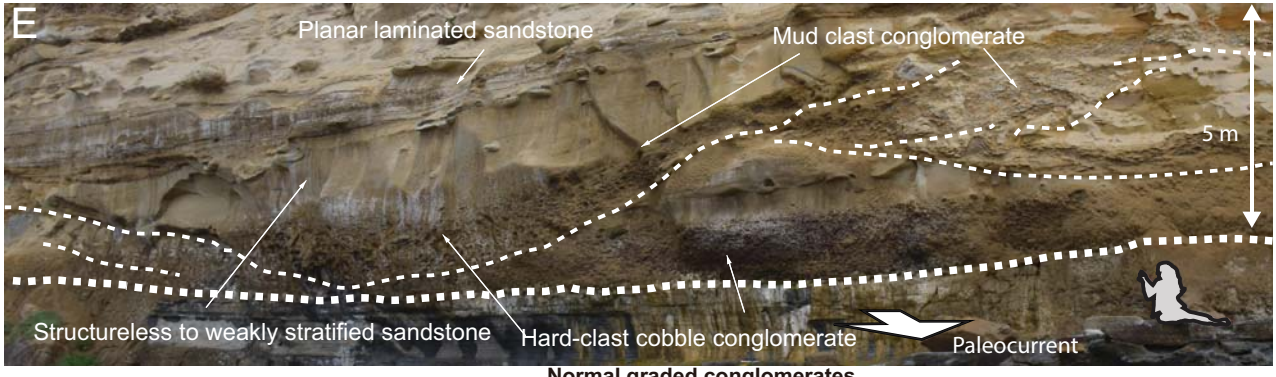

Normal graded conglomerates

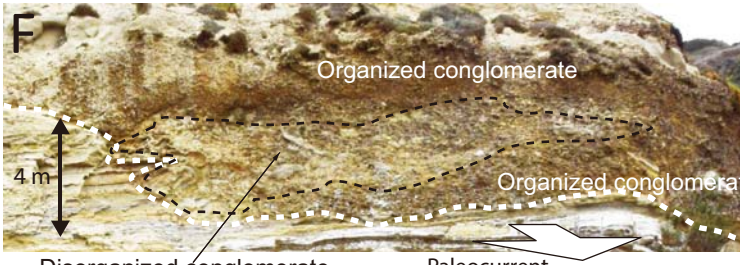

Highly irregular scour surface and disorganized conglomerate fill

A step-like erosion surface

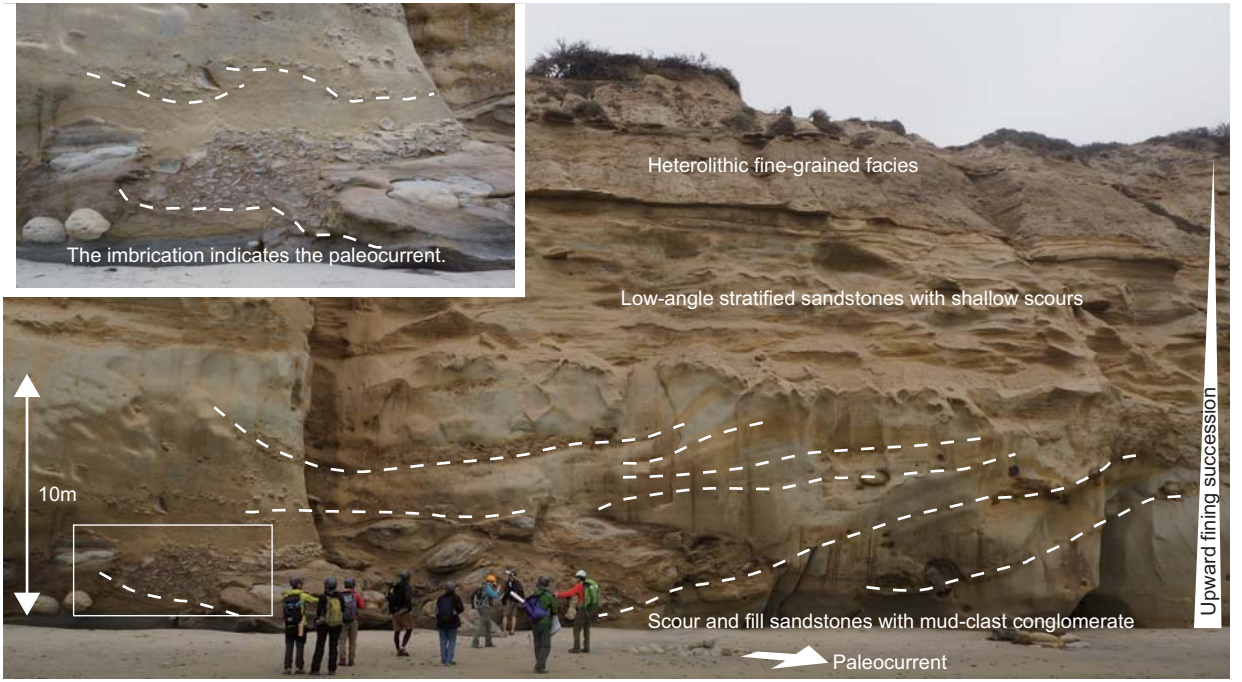
The imbrication indicates the paleocurrent.
Heterolithic fine-grained facies
Low-angle stratified sandstones with shallow scours
10m
Upward fining succession
Scour and fill sandstones with mud-clast conglomerate
Paleocurrent


A
3 m
Paleocurrent
B
Heterolithic fine-grained facies (Siltstone dominated)
Heterolithic fine-grained facies (Thinly bedded siltstone and sandstone dominated)
Sandstone
3 m
Paleocurrent
C
Flow
T=6.5[hr]